

Towards asteroseismology of core-collapse supernovae with gravitational-wave observations - II. Spacetime perturbations

Alejandro Torres-Forné^{1*}, Pablo Cerdá-Durán¹, Andrea Passamonti²,
Martin Obergaulinger¹ and José A. Font^{1,3}

¹*Departamento de Astronomía y Astrofísica, Universitat de València, C/ Dr. Moliner, 50, Burjassot (Valencia) E46100, Spain.*

²*Departamento de Física Aplicada, Universitat d'Alacant, Ap. Correos 99, E03080 Alicante, Spain.*

³*Observatori Astronòmic, Universitat de València, C/ Catedrático José Beltrán 2, 46980, Paterna (València), Spain.*

Accepted XXX. Received YYY; in original form ZZZ

ABSTRACT

Improvements in ground-based, advanced gravitational wave (GW) detectors may allow in the near future to observe the GW signal of a nearby core-collapse supernova. For the most common type of progenitors, likely with slowly rotating cores, the dominant GW emission mechanisms are the post-bounce oscillations of the proto-neutron star (PNS) before the explosion. We present a new procedure to compute the eigenmodes of the system formed by the PNS and the stalled accretion shock in general relativity including spacetime perturbations. The new method improves on previous results by accounting for perturbations of both the lapse function and the conformal factor. We apply our analysis to two numerical core-collapse simulations and show that our improved method is able to obtain eigenfrequencies that accurately match the features observed in the GW signal and to predict the qualitative behaviour of quasi-radial oscillations. Our analysis is possible thanks to a newly developed algorithm to classify the computed eigenmodes in different classes (f-, p-, and g-modes), improving previous results which suffered from misclassification issues. We find that most of the GW energy is stored in the lowest order eigenmodes, in particular in the 2g_1 mode and in the 2f mode. Our results also suggest that a low-frequency component of the GW signal attributed in previous works to the characteristic frequency of the Standing Accretion Shock Instability, should be identified as the fundamental quadrupolar f-mode. We also develop a formalism to estimate the contribution of quasi-radial ($l = 0$) modes to the quadrupolar component of the GW emission in the case of a deformed background, with application to rapidly rotating cores. This work provides further support for asteroseismology of core-collapse supernovae and the inference of PNS properties based on GW observations.

Key words: asteroseismology – gravitational waves – methods: numerical – stars: neutron – stars: oscillations – supernovae: general

1 INTRODUCTION

With the LIGO/Virgo discovery of gravitational waves (GWs) from a binary neutron star (BNS) merger and the subsequent follow-up observations across the electromagnetic spectrum by dozens of astronomical facilities and several neutrino telescopes, the field of multi-messenger astronomy has started (Abbott et al. 2017b). Significant advances toward explaining a number of open issues in relativistic as-

trophysics have been made thanks to the single observation of GW170817, from the mechanism behind short gamma-ray bursts (Abbott et al. 2017c) to the r -process-mediated nucleosynthesis of heavy elements in kilonovae (Abbott et al. 2017d), along with independent measures of cosmological parameters (Abbott et al. 2017a). Moreover, GWs from BNS mergers offer the opportunity to probe the properties high-density matter, yielding constraints on the neutron star radii and on the equation of state (EOS) (Annala et al. 2018; Fatoyev et al. 2018; De et al. 2018; Abbott et al. 2018).

A type of transient GW signal that remains to be detected is the one produced in core-collapse supernovae (CC-

* E-mail: alejandro.torres@uv.es

SNe), associated with the catastrophic collapse of the unstable iron cores that massive stars (from $\sim 8M_{\odot}$ to $\sim 100M_{\odot}$) develop at the end of their cycles of thermonuclear burning reactions. Collapsing stars produce rich and complex gravitational waveforms. When detected, those may provide important information about the phenomenology of the scenario, specially when combined with observations of their electromagnetic emission and neutrino emission. Their typical range of frequencies falls within the most sensitive region of the advanced LIGO and Virgo detectors. CCSNe are rare events, happening at rates of about one per century (see e.g. Gossan et al. 2016) observable within the Milky Way. This may explain why GWs from CCSNe have not yet been detected. In terms of signal amplitudes, it would be possible to detect magneto-rotational explosions up to ~ 5 Mpc (Gossan et al. 2016), but the event rate for such class of explosions is even lower, $\sim 10^{-4}\text{yr}^{-1}$ (less than 1% of all CCSNe, see discussion in Woosley & Bloom 2006). Despite this constraint, there have been attempts to detect the GW emission of supernova signals with the current network of detectors, either through techniques that search generic short-duration burst signals without targeting specific supernova events or with targeted searches that use the known sky-location and time window of electromagnetic or neutrino events (Thrane & Coughlin 2015; Klimentenko et al. 2016).

Unlike the case of BBH mergers, it is currently not possible to relate uniquely and unambiguously the properties of the progenitor stars (such as mass, rotation rate, metallicity, or magnetic fields) with the resulting waveforms. The reasons are diverse: (i) the complex non-linear dynamics associated with the evolution of a fluid interacting with neutrino radiation, (ii) the stochastic and chaotic behaviour of instabilities (both during and prior to the collapse of the star), (iii) the uncertainties in the stellar evolution of massive stars (specially regarding the treatment of convection, magnetic fields and angular momentum transport), and (iv) the uncertainties in the nuclear and weak interactions necessary for the high-density EOS and neutrino radiation, respectively.

In CCSN, GWs are produced during the hydrodynamical bounce and during the evolution of the instabilities that occur in the cavity formed by the newborn neutron star and the accretion shock. The violent dynamics excite different modes of oscillation of the proto-neutron star (PNS) and of its surroundings, including the shock wave. Most of the previous work on the field (Reisenegger & Goldreich 1992; Ferrari et al. 2003, 2004; Passamonti et al. 2005; Krüger et al. 2015; Sotani & Takiwaki 2016; Camelió et al. 2017) has focused in the computation of the oscillations modes of the PNS alone (without the interaction with the shock) and with a simplified background PNS model. In a previous paper (Torres-Forné et al. 2018) we studied the relationship between the spectrum of oscillations of the PNS - shock wave system after core bounce (analyzing linear perturbations in general relativity of this background system) and the characteristic GW frequencies obtained in numerical simulations. In particular, we showed that both spectra are closely related, which can be used to identify the oscillation modes of the PNS, such as the g -modes and the p -modes, obtaining a remarkable correspondence with the time-frequency distribution of the GW signal. This result showed that it is possible to perform CCSN asteroseismology and serves as a starting point to carry out inference of astrophysical param-

eters of PNS using the information contained in the gravitational waveforms to be detected in future observations of current or third-generation GW detectors. We note that these results have been recently extended by Morozova et al. (2018), who included spacetime perturbations in their analysis, albeit only of the lapse function, showing that spacetime perturbations have indeed an impact in the calculation.

In the current paper, we build on the approach presented in Torres-Forné et al. (2018) and incorporate to the methodology an augmented set of spacetime perturbation equations with respect to Morozova et al. (2018). The aim of this work is to understand the features observed in the GW signal of CCSN simulations, which have been interpreted as g -modes of the PNS (Murphy et al. 2009; Müller et al. 2013; Cerdá-Durán et al. 2013; Yakunin et al. 2015; Kuroda et al. 2016; Andresen et al. 2017). It also attempts to shed some light on the imprint of the standing accreting shock instability (SASI, Blondin et al. 2003; Foglizzo et al. 2007) in the GW signal observed in numerical simulations (Cerdá-Durán et al. 2013; Kuroda et al. 2016; Andresen et al. 2017). The paper is organised as follows: In Section 2 we develop our linear analysis formalism and estimate the GW emission for the case of a background deformed by rotation. In Section 3 we present the numerical methods used to solve the eigenvalue problem and the algorithms used in the classification of the eigenmodes. Section 4 presents our results and the comparison with the GW signal computed in the numerical simulations. Finally, in Section 5 we summarise our results and discuss their implications. The paper contains three appendices with technical details regarding numerical aspects. Throughout this paper we use a spacelike metric signature $(-, +, +, +)$ and $c = G = 1$ (geometrised) units, where c stands for the speed of light and G is Newton's gravitational constant. As customary, Greek indices run from 0 to 3, Latin indices from 1 to 3, and we use Einstein's summation convention for repeated indices.

2 LINEAR PERTURBATIONS OF A SPHERICALLY-SYMMETRIC BACKGROUND

We start our analysis with the description of the perturbations of a spherically-symmetric, self-gravitating, equilibrium configuration. The interested reader is addressed to Kokkotas & Schmidt (1999) and to Friedman & Stergioulas (2013) for detailed information on linear perturbations of compact stars and asteroseismology. Classically, this analysis was performed in Schwarzschild coordinates by Thorne & Campolattaro (1967). In our work we use isotropic coordinates instead, which are closer to the gauge condition used in the relativistic CCSN numerical simulation we employ for the comparison (Cerdá-Durán et al. 2013), which is based on the conformally-flat approximation (Isenberg 2008; Wilson et al. 1996). Moreover, the derivation of the equations in these coordinates also bears resemblance with the equations in the Newtonian case (see Reisenegger & Goldreich 1992), which makes it easier to identify the role of the different terms in the equations and to interpret the solutions. This choice of gauge also makes it straightforward to perform the mode analysis of the Newtonian simulations we make use of (Obergaulinger et al. 2018).

The metric in a 3 + 1 foliation of the space-time in coordinates (t, x^i) is

$$ds^2 = g_{\mu\nu} dx^\mu dx^\nu = (\beta^i \beta_i - \alpha^2) dt^2 + 2\beta_i dt dx^i + \gamma_{ij} dx^i dx^j, \quad (1)$$

where β^i is the shift 3-vector, α is the lapse function, and γ_{ij} is the spatial 3-metric.

In this work we consider the conformally flat condition approximation (CFC [Isenberg 2008](#); [Wilson et al. 1996](#)) of general relativity (GR). This approximation has some advantages for simulations of CCSNe: i) In spherical symmetry the CFC metric is exact and it is equivalent to choosing maximal slicing and isotropic coordinates; ii) In the post-Newtonian regime ($M/R < 1$) it deviates from GR as first post-Newtonian correction times the ellipticity squared ([Kley & Schäfer 1999](#); [Cordero-Carrión et al. 2009](#)); iii) Direct comparisons with full GR simulations of the collapse of rapidly rotating stellar cores have shown an excellent agreement in both the dynamics and the GW signal ([Shibata & Sekiguchi 2004](#); [Ott et al. 2007b,a](#)). Disagreement with GR has been estimated to be below 1% in those cases ([Cerdá-Durán et al. 2005](#)); iv) The resulting equations can be applied directly to the analysis of numerical simulations in the CFC approximation and, with minor modifications, to Newtonian simulations. v) In the Cowling approximation the coordinates coincide with those used in [Torres-Forné et al. \(2018\)](#), making possible a direct comparison with our previous results.

In CFC, the spatial 3-metric is conformally flat, $\gamma_{ij} = \psi f_{ij}$, where ψ is the conformal factor and f_{ij} is the spatial 3-metric. The Einstein equations for the CFC metric form a purely elliptic system given by

$$\nabla^2 \psi = -2\pi\psi^5 \left(E + \frac{K_{ij} K^{ij}}{16\pi} \right), \quad (2)$$

$$\nabla^2 Q = 2\pi Q \psi^4 \left(E + 2S + \frac{7K_{ij} K^{ij}}{16\pi} \right), \quad (3)$$

$$\nabla^2 \beta^i + \frac{1}{3} \nabla^i \nabla_j \beta^j = 16\pi\alpha\psi^4 S^i + 2\psi^{10} K^{ij} \nabla_j \left(\frac{\alpha}{\psi^6} \right), \quad (4)$$

where ∇^2 and ∇_i are the Laplacian and nabla operators with respect to the flat 3-metric, respectively, K^{ij} is the extrinsic curvature, and $Q \equiv \alpha\psi$. The energy-momentum content couples to the spacetime geometry through the projections of the energy-momentum tensor, $T_{\mu\nu}$, onto the 3 + 1 foliation

$$E \equiv \alpha^2 T^{00}, \quad S_i \equiv -\alpha^{-1} (T_{0i} - T_{ij} \beta^j), \quad (5)$$

$$S_{ij} \equiv T_{ij}, \quad S \equiv S_{ij} \gamma^{ij}. \quad (6)$$

We consider a perfect fluid, for which the energy-momentum tensor is given by

$$T^{\mu\nu} = \rho h u^\mu u^\nu + P g^{\mu\nu}, \quad (7)$$

where ρ is the rest-mass density, P is the pressure, u^μ is the 4-velocity, $h \equiv 1 + \epsilon + P/\rho$ is the specific enthalpy, and ϵ is the specific internal energy. It is useful to define the energy density as $e \equiv \rho(1 + \epsilon)$.

The mass-conservation (continuity) and momentum

conservation equations in GR read ([Banyuls et al. 1997](#)):

$$\frac{1}{\sqrt{\gamma}} \partial_t [\sqrt{\gamma} D] + \frac{1}{\sqrt{\gamma}} \partial_i [\sqrt{\gamma} D v^{*i}] = 0, \quad (8)$$

$$\frac{1}{\sqrt{\gamma}} \partial_t [\sqrt{\gamma} S_j] + \frac{1}{\sqrt{\gamma}} \partial_i [\sqrt{\gamma} S_j v^{*i}] + \alpha \partial_j P = \frac{\alpha \rho h}{2} u^\mu u^\nu \partial_j g_{\mu\nu}, \quad (9)$$

where γ is the determinant of the three-metric. The conserved quantities are $D = \rho W$ and $S_j = \rho h W^2 v_j$, where $W = 1/\sqrt{1 - v_i v^i}$ is the Lorentz factor. The Eulerian and “advective” velocities are, respectively,

$$v^i = \frac{u^i}{W} + \frac{\beta^i}{\alpha}, \quad v^{*i} = \frac{u^i}{u^0} = \alpha v^i - \beta^i. \quad (10)$$

Let us consider a solution of the hydrodynamics equations that is in equilibrium ($\partial_t = 0$) and is static ($v^i = 0$). In this case the metric equations (Eqs. 2-4) and the hydrodynamics equations (Eqs. (8)-(9)) reduce to

$$\nabla^2 \psi = -2\pi\psi^5 E, \quad (11)$$

$$\nabla^2 Q = 2\pi Q \psi^4 (E + 2S), \quad (12)$$

$$\frac{1}{\rho h} \partial_i P = -\partial_i \ln \alpha \equiv \mathcal{G}_i, \quad (13)$$

and $\beta^i = 0$. In the Newtonian limit \mathcal{G}_i is the gravitational acceleration, whose only non-zero component is $\mathcal{G}_r \equiv \mathcal{G}$. The solution of Eqs. (11)-(13) corresponds to the unperturbed state or background solution.

Following [Torres-Forné et al. \(2018\)](#), we consider linear adiabatic perturbations of the hydrodynamics equations with respect to the background equilibrium configuration. We use the same notation and denote the Eulerian perturbations of the different quantities with δ (e.g. $\delta\rho$) and without it for the background quantities (e.g. ρ). Our previous work was based on the Cowling approximation. Here, we consider the general case including also the metric perturbations, namely $\delta\alpha$, $\delta\psi$, and $\delta\beta^j$. For a weak gravitational field ($M/R \ll 1$), the leading term in the post-Newtonian expansion of the metric contributes only to α , while the first correction to ψ and β^i appears at the first post-Newtonian level ([Blanchet et al. 1990](#)). Therefore, for the mildly relativistic gravitational field of a PNS, we expect $\delta\alpha$ to be dominant in front of $\delta\psi$ and $\delta\beta^i$. In this work we consider $\delta\beta^i = 0$, which simplifies the equations significantly. Although this approach does not fully include the metric perturbations, it allows us to assess the effect of 1PN corrections with respect to a “Newtonian-like” approach in which only $\delta\alpha$ is considered, as in [Morozova et al. \(2018\)](#).

We denote as ξ^i the Lagrangian displacement of a fluid element with respect to its position at rest. Its value is related to the advective velocity as

$$\partial_t \xi^i = \delta v^{*i}. \quad (14)$$

The Lagrangian perturbation of any quantity, e.g. ρ , is related to the Eulerian perturbations as

$$\Delta\rho = \delta\rho + \xi^i \partial_i \rho. \quad (15)$$

The linearised version of Eqs. (8) and (9) are

$$\frac{\Delta\rho}{\rho} = -\left(\partial_i \xi^i + \xi^i \partial_i \ln \sqrt{\gamma} \right) - 6 \frac{\delta\psi}{\psi}, \quad (16)$$

$$\rho h \partial_t \delta v_i + \alpha \partial_t \delta P = -\delta(\rho h) \partial_i \alpha - \rho h (\partial_i \delta\alpha - \delta\alpha \partial_i \ln \alpha). \quad (17)$$

We use spherical coordinates, $\{r, \theta, \varphi\}$, in which $\sqrt{\gamma} =$

$\psi^6 r^2 \sin \theta$. The condition of adiabaticity of the perturbations implies that

$$\frac{\Delta P}{\Delta \rho} = \left. \frac{\partial P}{\partial \rho} \right|_{\text{adiabatic}} = hc_s^2 = \frac{P}{\rho} \Gamma_1, \quad (18)$$

where c_s is the relativistic speed of sound and Γ_1 is the adiabatic index. This allows us to write

$$\delta(\rho h) = \left(1 + \frac{1}{c_s^2}\right) \delta P - \rho h \xi^i \mathcal{B}_i, \quad (19)$$

where

$$\mathcal{B}_i \equiv \frac{\partial_i e}{\rho h} - \frac{1}{\Gamma_1} \frac{\partial_i P}{P}, \quad (20)$$

is the relativistic version of the Schwarzschild discriminant. Since the background is spherically symmetric, the only non-zero component is $\mathcal{B}_r \equiv \mathcal{B}$.

The radial and angular parts of Eq. (17) are given by

$$\rho h \psi^4 \alpha^{-2} \frac{\partial^2 \xi^r}{\partial t^2} + \partial_r \delta P = \delta(\rho h) \mathcal{G} - \rho h \alpha^{-1} (\partial_r \delta \alpha + \delta \alpha \mathcal{G}), \quad (21)$$

$$\rho h \psi^4 \alpha^{-2} r^2 \frac{\partial^2 \xi^\theta}{\partial t^2} + \partial_\theta \delta P = -\rho h \alpha^{-1} \partial_\theta \delta \alpha, \quad (22)$$

$$\rho h \psi^4 \alpha^{-2} r^2 \sin^2 \theta \frac{\partial^2 \xi^\varphi}{\partial t^2} + \partial_\varphi \delta P = -\rho h \alpha^{-1} \partial_\varphi \delta \alpha, \quad (23)$$

where we have used that, in the coordinate basis, the covariant components of the velocity are given by $\delta v_r = \psi^4 \delta v^r$, $\delta v_\theta = r^2 \psi^4 \delta v^\theta$ and $\delta v_\varphi = r^2 \sin^2 \theta \psi^4 \delta v^\varphi$.

Additionally we need equations for the metric perturbations $\delta \hat{\psi}$ and $\delta \hat{Q}$, that can be obtained by linearising Eqs. (2)-(3) and subtracting the background solution (Eqs. (11)-(12)),

$$\nabla^2 \delta \psi = -10\pi e \psi^4 \delta \psi - 2\pi \psi^5 \left[\frac{\delta P}{c_s^2} - \rho h \xi^r \mathcal{B} \right], \quad (24)$$

$$\begin{aligned} \nabla^2 \delta Q = & 2\pi(\rho h + 5P) \psi^4 (\delta Q + 4\alpha \delta \psi) \\ & + 2\pi \alpha \psi^5 \left[\left(6 + \frac{2}{c_s^2}\right) \delta P - \rho h \xi^r \mathcal{B} \right], \end{aligned} \quad (25)$$

where we have used that $\delta K^{ij} = 0$, for $\delta \beta^i = 0$.

We perform an expansion of the perturbations with a harmonic time dependence of frequency σ and a spherical-harmonic expansion for the angular dependence

$$\delta P = \delta \hat{P} Y_{lm} e^{-i\sigma t}, \quad (26)$$

$$\xi^r = \eta_r Y_{lm} e^{-i\sigma t}, \quad (27)$$

$$\xi^\theta = \eta_\perp \frac{1}{r^2} \partial_\theta Y_{lm} e^{-i\sigma t}, \quad (28)$$

$$\xi^\varphi = \eta_\perp \frac{1}{r^2 \sin^2 \theta} \partial_\varphi Y_{lm} e^{-i\sigma t}, \quad (29)$$

and all scalar quantities (e.g. δQ and $\delta \psi$) in an equivalent way to δP . The quantities η_r, η_\perp and the scalar perturbations with the hat (e.g. $\delta \hat{P}$, $\delta \hat{Q}$ and $\delta \hat{\psi}$), depend on the radial coordinate only.

2.1 Non-radial perturbations ($l \neq 0$)

For $l \neq 0$, by inserting the spherical-harmonic expansion into equations (21)-(22) we obtain:

$$-\sigma^2 q \eta_r + \partial_r \delta \hat{P} = \delta \hat{\rho h} \mathcal{G} - \rho h \alpha^{-1} (\partial_r \delta \hat{\alpha} + \mathcal{G} \delta \hat{\alpha}), \quad (30)$$

$$-\sigma^2 q \eta_\perp + \delta \hat{P} = -\rho h \alpha^{-1} \delta \hat{\alpha}, \quad (31)$$

where for convenience we have defined $q \equiv \rho h \alpha^{-2} \psi^4$. From Eq. (31) it follows that

$$\delta \hat{P} = q \sigma^2 \eta_\perp - \frac{\rho h}{\alpha} \delta \hat{\alpha} = q \sigma^2 \eta_\perp + \rho h \left(\frac{\delta \hat{\psi}}{\psi} - \frac{\delta \hat{Q}}{Q} \right). \quad (32)$$

Using Eqs. (32) and (19) to simplify Eqs. (16) and (30) we obtain

$$\begin{aligned} \partial_r \eta_r + \left[\frac{2}{r} + \frac{1}{\Gamma_1} \frac{\partial_r P}{P} + 6 \frac{\partial_r \psi}{\psi} \right] \eta_r + \frac{\psi^4}{\alpha^2 c_s^2} (\sigma^2 - \mathcal{L}^2) \eta_\perp \\ = \frac{1}{c_s^2} \frac{\delta \hat{Q}}{Q} - \left(6 + \frac{1}{c_s^2} \right) \frac{\delta \hat{\psi}}{\psi}, \end{aligned} \quad (33)$$

$$\begin{aligned} \partial_r \eta_\perp - \left(1 - \frac{\mathcal{N}^2}{\sigma^2} \right) \eta_r + \left[\partial_r \ln q - \mathcal{G} \left(1 + \frac{1}{c_s^2} \right) \right] \eta_\perp \\ = \frac{\alpha^2}{\psi^4 \sigma^2} \left[\partial_r (\ln \rho h) - \left(1 + \frac{1}{c_s^2} \right) \mathcal{G} \right] \left(\frac{\delta \hat{Q}}{Q} - \frac{\delta \hat{\psi}}{\psi} \right), \end{aligned} \quad (34)$$

where \mathcal{L} is the relativistic Lamb frequency defined as

$$\mathcal{L}^2 \equiv \frac{\alpha^2}{\psi^4} c_s^2 \frac{l(l+1)}{r^2}, \quad (35)$$

and \mathcal{N} is the relativistic Brunt-Väisälä frequency

$$\mathcal{N}^2 \equiv \frac{\alpha^2}{\psi^4} \mathcal{G}^i \mathcal{B}_i = \frac{\alpha^2}{\psi^4} \mathcal{B} \mathcal{G}. \quad (36)$$

Eqs. (24)-(25) for the metric perturbations can also be simplified using Eq. (32). After the spherical harmonic expansion they read

$$\begin{aligned} \hat{\nabla}^2 \delta \hat{\psi} = & -2\pi \psi^5 \left[\left(5e + \frac{\rho h}{c_s^2} \right) \frac{\delta \hat{\psi}}{\psi} - \frac{\rho h}{c_s^2} \frac{\delta \hat{Q}}{Q} \right] \\ & - 2\pi \rho h \psi^5 \left(\frac{\psi^4 \sigma^2}{\alpha^2 c_s^2} \eta_\perp - \mathcal{B} \eta_r \right), \end{aligned} \quad (37)$$

$$\begin{aligned} \hat{\nabla}^2 \delta \hat{Q} = & 2\pi(\rho h + 5P) \alpha \psi^5 \left(\frac{\delta \hat{Q}}{Q} + 4 \frac{\delta \hat{\psi}}{\psi} \right) \\ & + 2\pi \rho h \alpha \psi^5 \left[\left(6 + \frac{1}{c_s^2} \right) \left(\frac{\psi^4 \sigma^2}{\alpha^2} \eta_\perp - \frac{\delta \hat{Q}}{Q} + \frac{\delta \hat{\psi}}{\psi} \right) - \eta_r \mathcal{B} \right], \end{aligned} \quad (38)$$

where

$$\hat{\nabla}^2 \equiv \partial_{rr} + \frac{2}{r} \partial_r - \frac{l(l+1)}{r^2}. \quad (39)$$

The system of Eqs. (33), (34), (37) and (38) can be reduced to a system of 6 first-order ODEs by introducing the variables $K \equiv \partial_r \delta \hat{Q}$ and $\Psi \equiv \partial_r \delta \hat{\psi}$. The resulting system of equations can be written in compact form as

$$\partial_r \mathbf{u} = \mathbf{A} \mathbf{u}, \quad (40)$$

where $\mathbf{u} \equiv (\eta_r, \eta_\perp, K, \delta \hat{Q}, \Psi, \delta \hat{\psi})^T$ and \mathbf{A} is a 6×6 coefficient matrix whose components are explicitly written in appendix A.

2.2 Radial perturbations ($l = 0$)

In non-rotating stars, the Lagrangian displacement of radial oscillations has $\xi^\theta = \xi^\varphi = 0$, i.e. $\eta_\perp = 0$. This case cannot be treated as a particular case of the general derivation for

$l \neq 0$ (previous section). In this case, the continuity and momentum equations are

$$\frac{\delta\hat{\rho}}{\rho} = -\partial_r\eta_r - \left(\frac{2}{r} + \frac{\partial_r\rho}{\rho} + 6\frac{\partial_r\psi}{\psi}\right)\eta_r - 6\frac{\delta\hat{\psi}}{\psi}, \quad (41)$$

$$-\sigma^2 q\eta_r + \partial_r\delta\hat{P} = \mathcal{G}\delta\hat{\rho}h - \rho h\alpha^{-1}(\partial_r\delta\hat{\alpha} + \delta\hat{\alpha}\mathcal{G}). \quad (42)$$

From Eqs. (18) and (19) the various scalar perturbations are given by

$$\delta\hat{P} = P\Gamma_1 \left[\frac{\delta\hat{\rho}}{\rho} + \eta_r \left(\frac{\partial_r\rho}{\rho} - \frac{\partial_r P}{\Gamma_1 P} \right) \right], \quad (43)$$

$$\delta\hat{\rho}h = \left(1 + \frac{1}{c_s^2}\right)\delta\hat{P} - \rho h\eta_r \mathcal{B}. \quad (44)$$

Combining Eqs. (41)-(44) we obtain the following equations for η_r and $\delta\hat{P}$

$$\partial_r\eta_r + \left[\frac{2}{r} + \frac{1}{\Gamma_1} \frac{\partial_r P}{P} + 6\frac{\partial_r\psi}{\psi}\right]\eta_r + \frac{1}{P\Gamma_1}\delta\hat{P} = -6\frac{\delta\hat{\psi}}{\psi}, \quad (45)$$

$$\partial_r\delta\hat{P} + q(N^2 - \sigma^2)\eta_r - \mathcal{G}\left(1 + \frac{1}{c_s^2}\right)\delta\hat{P} = -\rho h\alpha^{-1}(\partial_r\delta\hat{\alpha} + \delta\hat{\alpha}\mathcal{G}). \quad (46)$$

Using Eqs. (24) and (25) the metric perturbations are

$$\hat{\nabla}^2\delta\hat{\psi} = -10\pi e\psi^4\delta\hat{\psi} - 2\pi\psi^5\left[\frac{\delta\hat{P}}{c_s^2} - \rho h\eta_r\mathcal{B}\right], \quad (47)$$

$$\hat{\nabla}^2\delta\hat{Q} = 2\pi(\rho h + 5P)\psi^4(\delta\hat{Q} + 4\alpha\delta\hat{\psi}) + 2\pi\alpha\psi^5\left[\left(6 + \frac{2}{c_s^2}\right)\delta\hat{P} - \rho h\eta_r\mathcal{B}\right]. \quad (48)$$

Similarly to the case with $l \neq 0$, the system of Eqs. (45)-(48) can be written as a system of 6 first-order ODEs by using K and Ψ and cast in the same compact form as Eq. (40), where in this case $\mathbf{u} \equiv (\eta_r, \delta\hat{P}, K, \delta\hat{Q}, \Psi, \delta\hat{\psi})^T$ and \mathbf{A} is a 6×6 coefficient matrix whose components are explicitly given in appendix A.

2.3 Boundary conditions

As in Torres-Forné et al. (2018), we impose zero-displacement boundary conditions at the shock location

$$\xi_r|_{\text{shock}} = 0 \quad \rightarrow \quad \eta_r|_{\text{shock}} = 0, \quad (49)$$

which is a consequence of the impossibility of perturbations to propagate across the shock from the subsonic to the supersonic region. At the origin ($r = 0$) we impose regularity, which for $l \neq 0$ (see Reisenegger & Goldreich 1992) results in¹

$$\eta_r|_{r=0} = \frac{l}{r}\eta_\perp|_{r=0} \propto r^{l-1}, \quad (50)$$

and for $l = 0$ in

$$\eta_r|_{r=0} \propto r, \quad (51)$$

$$\delta\hat{P}|_{r=0} = -P\Gamma_1 \left[6\frac{\delta\hat{\psi}}{\psi} + \frac{\eta_r}{r} \right]_{r=0}. \quad (52)$$

¹ Note that in Torres-Forné et al. (2018) there is a missing r factor in the text (but not in the calculations).

The latter expression has been obtained by evaluating Eq. (45) at $r = 0$ and imposing the boundary condition for η_r given by Eq. (51).

Regarding metric perturbations, regularity at $r = 0$ implies that

$$K|_{r=0} = \frac{l}{r}\delta\hat{Q}|_{r=0} \propto r^{l-1} \quad ; \quad \Psi|_{r=0} = \frac{l}{r}\delta\hat{\psi}|_{r=0} \propto r^{l-1}. \quad (53)$$

As a consequence all four metric functions are zero at $r = 0$ for $l \geq 2$.

Outside the sources ($\rho = 0$) the metric perturbations fulfil $\hat{\nabla}^2\delta\hat{\psi} = 0$ and $\hat{\nabla}^2\delta\hat{Q} = 0$ and hence the solution decays as $r^{-(l+1)}$. Outside the shock, density is non zero but, since $\eta_r = \eta_\perp = 0$, and $\delta\hat{Q}$ and $\delta\hat{\psi}$ decay radially, it can be shown that, sufficiently far away from the shock (but still inside the star), the solution also decays as $r^{-(l+1)}$. For simplicity and given that outside the shock there is a considerable drop in density, we impose this behaviour at the shock location. As a consequence

$$[K + (l+1)\delta\hat{Q}/r]_{\text{shock}} = 0, \quad (54)$$

$$[\Psi + (l+1)\delta\hat{\psi}/r]_{\text{shock}} = 0. \quad (55)$$

We note that these boundary conditions differ with respect to those used by Morozova et al. (2018), which impose boundary conditions at the PNS surface, assuming it is a free surface ($\Delta P = 0$).

2.4 Gravitational wave emission

2.4.1 Spherical background

Let us consider a general linear perturbation of the spherically-symmetric background considered in the previous sections as a combination of eigenfunctions, which we denote hereafter as $\delta\rho_{lm}$ (and so forth for other perturbed quantities):

$$\delta\rho = \sum_{l=2}^{\infty} \sum_{m=-l}^{+l} \delta\rho_{lm} = \sum_{l=2}^{\infty} \sum_{m=-l}^{+l} \delta\hat{\rho}_{lm} Y_{lm}, \quad (56)$$

where $\delta\hat{\rho}_{lm}$ can be computed as

$$\delta\hat{\rho}_{lm} \approx \rho \left(\frac{N^2}{\mathcal{G}} \eta_r^{lm} + \frac{\sigma^2}{c_s^2} \eta_\perp^{lm} \right). \quad (57)$$

In the Newtonian limit, the energy stored in all the (l, m) modes with a certain amplitude can be approximated as

$$E_{lm} = \frac{\sigma^2}{2} \int_0^{r_{\text{shock}}} \mathcal{E}_{lm} r^2 dr, \quad (58)$$

where \mathcal{E}_{lm} is the eigenmode energy density defined as

$$\mathcal{E}^{lm}(r) = \rho \left[\eta_r^{lm}(r)^2 + l(l+1) \frac{\eta_\perp^{lm}(r)^2}{r^2} \right]. \quad (59)$$

The (l, m) -mass multipole moment ($l \geq 2$) can be defined as

$$\delta D_{lm} \equiv \int dV r^l \delta\rho Y_{lm}^* = \int_0^{r_{\text{shock}}} r^{l+2} \delta\hat{\rho}_{lm} dr. \quad (60)$$

As a consequence, only the (l, m) mode contributes to δD_{lm} . As we address in the next section, this is a direct consequence of considering a spherically symmetric background.

Following [Thorne \(1969\)](#), it is possible to compute the radiated power in GWs as,

$$P_{lm} = \frac{G}{8\pi c^{2l+1}} \frac{(l+1)(l+2)}{(l-1)l} \left[\frac{4\pi\sigma^{l+1}}{(2l+1)!!} \right]^2 \left(|\delta D_{lm}|^2 + \frac{1}{c^2} |\delta J_{lm}|^2 \right), \quad (61)$$

where δJ_{lm} are the current multipoles and we show the factors c and G explicitly for the sake of the discussion.

The dominant GW emission channel is the mass quadrupole ($l = 2$). The contribution by higher-order mass multipoles and current multipoles is suppressed by at least a factor $1/c^2$ and is not relevant for GW detection. The implication is that, if the background is spherically symmetric, only $l = 2$ oscillation modes are relevant for GW emission, and the radiated power of the relevant modes can be computed as

$$P_{2m} = \frac{G}{c^5} \frac{4\pi\sigma^6}{75} |\delta D_{2m}|^2. \quad (62)$$

The amplitude of the GW emitted for $(l, m) = (2, 0)$ modes can be computed as

$$h_+ = -\frac{1}{D} \sin^2 \Theta \frac{8\pi}{5} \sigma^2 \delta D_{20}, \quad (63)$$

$$h_\times = 0, \quad (64)$$

where D is the distance to the source and Θ is the observation angle with respect to the symmetry axis of the mode.

In order to compare the power emitted by different modes with $l = 2$, we define the GW emission efficiency as

$$(\text{GW efficiency}) = \frac{P}{Ef}, \quad (65)$$

where f is the frequency of the mode. This equation gives an idea of the fraction of the mode energy radiated in GWs per oscillation cycle.

2.4.2 Deformed background

One of the limitations of our linear analysis is that is only applicable if the background is spherically symmetric. However, in the collapse of rapidly rotating cores, deformations in the star induced by rotation are known to enhance considerably the GW emission, increasing the wave amplitude by a factor 10 – 1000 (see e.g. [Fryer & New 2011](#)). Another motivation to consider a deformed background is the possible presence of $l = 0$ (quasi-radial) modes in the GW signal. [Cerdá-Durán et al. \(2013\)](#) noted that some of the features observed in the GW signal of their simulation could be explained by a $l = 0$ mode. As we show next, the presence of a deformed background allows for modes with $l \neq 2$ to contribute to the dominant GW channel ($l = 2$).

Let us consider an axisymmetric background of the form

$$\rho(r, \theta) = \rho_0(r) + a\tilde{\rho}_2(r)Y_{20}(\theta), \quad (66)$$

where ρ_0 is the spherically-symmetric contribution to the background, $\tilde{\rho}_2$, whose volume integral is normalised to unity, gives the radial dependence of the quadrupolar deformation, and a is a parameter controlling the amount of deformation ($a = 0$ corresponds to the spherically symmetric case

considered above). We consider only quadrupolar deformations of the background because those produce the strongest coupling between modes with $l \neq 2$ and the quadrupolar component of the GW signal. This allows us to compute the leading contribution to the signal. For simplicity, we consider $a \ll 1$. In particular we assume that the quadrupolar deformations are sufficiently small to be neglected when compared to the perturbations themselves, i.e.

$$a\tilde{\rho}_2 \ll \delta\rho_{2m} \ll \rho_0. \quad (67)$$

This allows to compute the leading-order contribution to the GW signal of modes with $l \neq 2$, without the added complexity of the linear analysis including rotation.

Under these conditions, the equations for the linear perturbations are identical to the equations for the spherical background. This means that we can use the eigenvalues and eigenfunctions already computed to estimate the leading-order contribution to the GW signal. The only necessary step is to compute the contribution of modes with $l \neq 2$ to the mass quadrupole δD_{2m} .

Since $a \ll 1$, we can consider that the new background can be described as a continuous deformation of the spherically symmetric background given by ρ_0 . This deformation can be described by a displacement vector X^i defined such that, for surfaces of constant density, corresponds to a Lagrangian perturbation

$$a\tilde{\rho}_2 Y_{20} + X^i \partial_i \rho_0 = 0. \quad (68)$$

Since the deformation is proportional to Y_{20} , X^i is purely radial, i.e. $X^r = N^r(r)Y_{20}$ and $X^\theta = X^\varphi = 0$. Note that this only happens for quadrupolar deformations of the background and simplifies significantly the analysis. Substituting in Eq. (68) one arrives to

$$N^r(r) = -\frac{a\tilde{\rho}_2}{\partial_r \rho_0}. \quad (69)$$

Let us consider a new set of coordinates (r', θ', φ') defined by

$$r' \equiv r + X^r = r + N^r Y_{20} \quad ; \quad \theta' \equiv \theta \quad ; \quad \varphi' \equiv \varphi. \quad (70)$$

By construction, in the new coordinates $\rho(r, \theta) = \rho(r')$, i.e. they are adapted to the deformation. Using Eq. (69) we can write

$$dr' = (1 + \partial_r N^r Y_{20}) dr \quad ; \quad d\theta' = d\theta \quad ; \quad d\varphi' = d\varphi, \quad (71)$$

which allows us to write the line element as

$$dl^2 \approx (1 - 2\partial_r N^r Y_{20}) dr'^2 + r'^2 \left(1 - \frac{2N^r Y_{20}}{r'} \right) d\Omega'^2, \quad (72)$$

where we have used that $X^r/r \ll 1$ and we have neglected higher order corrections. Here $d\Omega' \equiv \sin\theta' d\theta' d\varphi'$. Finally, the volume element in the new coordinates reads

$$dV \approx \left[1 - 2 \left(\partial_r N^r + \frac{N^r}{r'} \right) Y_{20} \right] r'^2 dr' d\Omega'. \quad (73)$$

Therefore, using the fact that the eigenfunctions and eigenvalues are unchanged at this level of approximation, we can compute the mass quadrupole by considering the change in the volume element in Eq. (60). The resulting contribution to the mass quadrupole of a mode with (l', m')

is

$$\begin{aligned} \delta D_{2m,l'm'} &= \int dV r^2 \delta \hat{\rho} Y_{l'm'} Y_{lm}^* \\ &\approx \int \left[1 - 2 \left(\partial_r N^r + \frac{N^r}{r'} \right) Y_{20} \right] r'^2 dr' d\Omega' \delta \hat{\rho} Y_{l'm'} Y_{lm}^*. \end{aligned} \quad (74)$$

For oscillation modes with $l' = 2$

$$\delta D_{2m,2m'} = \delta_{mm'} \int_0^{r_{\text{shock}}} r'^4 \delta \hat{\rho}_{2m'} dr' + O(a), \quad (75)$$

which is equivalent to the case with spherical background given by Eq. (60). However, for $l' \neq 2$, which gives a negligible contribution to the GW signal for the spherical background, we now obtain a non-zero contribution given by

$$\begin{aligned} \delta D_{2m,l'm'} &= \int r'^4 dr' d\Omega' \left(2\partial_r N^r + 4\frac{N^r}{r'} \right) \delta \hat{\rho}_{l'm'} Y_{20} Y_{l'm'} Y_{2m}^* \\ &+ O(a^2), \end{aligned} \quad (76)$$

The angular part of the integral can be easily computed (Arfken & Weber 1995), and the only non-zero contributions are

$$\delta D_{20,00} = \delta \hat{D}_{00}, \quad (77)$$

$$\delta D_{20,40} = \frac{6}{7} \delta \hat{D}_{40}, \quad (78)$$

$$\delta D_{2\pm 1,4\pm 1} = \frac{\sqrt{30}}{7} \delta \hat{D}_{4\pm 1}, \quad (79)$$

$$\delta D_{2\pm 2,4\pm 2} = \frac{\sqrt{15}}{7} \delta \hat{D}_{4\pm 2}, \quad (80)$$

where

$$\delta \hat{D}_{l'm'} \equiv \frac{1}{\sqrt{4\pi}} \int_0^{r_{\text{shock}}} r'^4 \left(2\partial_r N^r + 4\frac{N^r}{r'} \right) \delta \hat{\rho}_{l'm'} dr'. \quad (81)$$

Note that these integrals are independent of m' , except for the mode amplitude, which can be different for each m' . We can extract some conclusions from these results: i) the only oscillation modes contributing to the quadrupolar GW emission are those with $l' = 0, 2, 4$, and ii) modes with m' only produce GW in the $(2, m')$ channel. We will focus next on the contribution by $\delta D_{20,00}$ and $\delta D_{20,40}$, since the remaining contributions are just proportional to the latter.

In order to use Eq. (77-81) to compute the GW power of $l = 2, 4$ modes in a deformed background, one needs to compute $\tilde{\rho}_2$ from the original multidimensional simulation. To simplify this process and develop our intuition about the meaning of the corrections due to the deformation we will make some assumptions. Let us consider the deformation at a fixed radius r . The polar and equatorial radius of the density isocontour corresponding to $\rho_0(r)$ are given by:

$$r_e = r + b, \quad (82)$$

$$r_p = r - 2b, \quad (83)$$

$$b \equiv -\sqrt{\frac{5}{16\pi}} N^r. \quad (84)$$

The ellipticity of the system at this radius, considering an oblate form ($r_p < r_e$) is

$$e \equiv \sqrt{1 - \frac{r_p^2}{r_e^2}} = \frac{\sqrt{3b(2r-b)}}{r+b}. \quad (85)$$

To simplify further, we consider constant ellipticity at different radii. From Eqs. (84) and (85) this implies that

$$N^r = -\sqrt{\frac{16\pi}{5} \frac{(3-e^2) - 3\sqrt{1-e^2}}{3+e^2}} r, \quad (86)$$

such that, for $e = 0$ (spherical) it results $N^r = 0$. Using this expression, the integral needed to compute the contribution to the mass quadrupole is

$$\delta \hat{D}_{l'm'} \equiv -\sqrt{\frac{4}{5} \frac{(3-e^2) - 3\sqrt{1-e^2}}{3+e^2}} \int_0^{r_{\text{shock}}} r'^4 \delta \hat{\rho}_{l'm'} dr'. \quad (87)$$

Note that the integral is the same as for $l = 2$ modes, but using the corresponding multipole.

3 EIGENMODE CALCULATION

3.1 Background models

To test the capabilities of linear perturbation analysis we compute the eigenmodes for two CCSN simulations, for which we have all quantities necessary for the analysis and the GW signal, which is used for comparison.

Model s20 is the result of a simulation of the core collapse of a star of $20M_\odot$ of solar metallicity (Woosley & Heger 2007) with non-zero, but dynamically negligible, rotational velocity and magnetic field that was studied by Obergaullinger et al. (2018). The simulation was performed in axisymmetry using the ALCAR/Aenus code (Just et al. 2015) combining special relativistic magnetohydrodynamics, an approximately general relativistic gravitational potential (version ‘A’ of the TOV potential of Marek et al. (2006)), the SFHo EOS (Steiner et al. 2013), and an energy-dependent, two-moment, neutrino transport scheme. The core does not launch a supernova explosion. The mass of the PNS increases continuously due to the ongoing mass accretion, but does not exceed the threshold for collapse to a black hole during the first second after core bounce.

Model 35OC is a 2D core-collapse simulation performed by Cerdá-Durán et al. (2013) using the general-relativistic code CoCoNuT (Dimmelmeier et al. 2002, 2005). The progenitor is a low-metallicity $35M_\odot$ star at zero-age main-sequence from Woosley & Heger (2006). This progenitor has a high rotation rate and is usually regarded as a progenitor of long-duration gamma-ray bursts (GRBs). The simulation used the LS220 EOS of Lattimer & Swesty (1991) to describe matter at high density along with a simplified leakage scheme to approximate neutrino transport. This model does not produce a supernova explosion. Instead, the PNS becomes unstable to radial perturbations and collapses to a black hole 1.6 s after bounce.

Fig. 1 shows the time evolution of the location of the shock, the PNS surface and the outer boundary of the inner core for both simulations. We define the *shock* as the location where the flow becomes subsonic, the *PNS surface* as the radius at which $\rho = 10^{11} \text{ g cm}^{-3}$, and the *inner core* as the region where $\Gamma_1 > 2$, which is a good tracer of the region where the transition to nuclear matter has occurred.

3.2 Numerical integration

For the numerical calculation of the eigenmodes (“modes” hereafter) we follow a similar procedure as in Torres-Forné

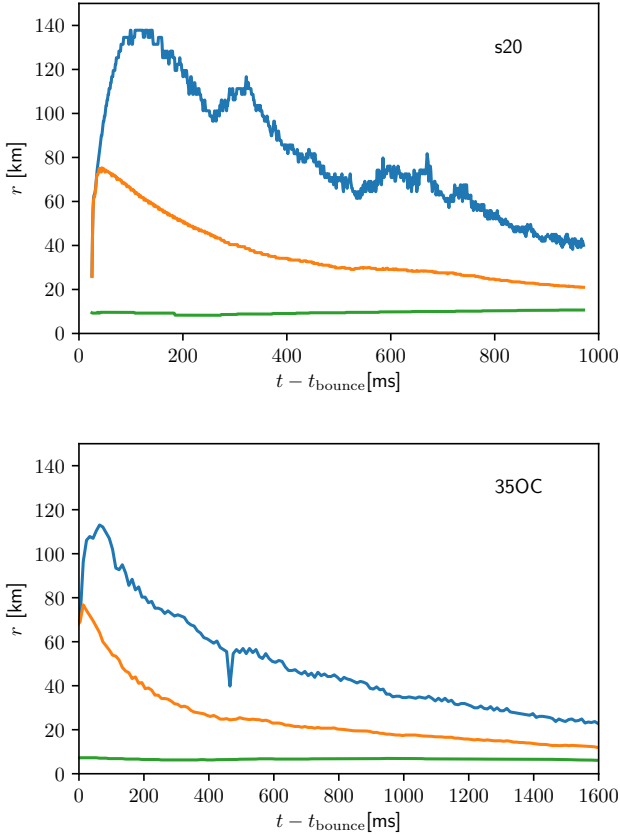


Figure 1. Time evolution of the location of the shock (blue), the surface of the PNS (orange) and the inner core (green), for models *s20* (upper panel) and *35OC* (bottom panel).

et al. (2018), i.e. we solve the perturbation equations for different values of σ , and then search for the values of σ with vanishing radial displacement at the shock ($\eta_r|_{\text{shock}} = 0$), by means of a bisection algorithm. The perturbation equations differ depending if $l = 0$ or $l \neq 0$, but in both cases the system can be cast as in Eq. (40). We integrate this system of six coupled ODEs outwards from the center to the shock radius. The integration is performed using a second-order implicit method (trapezoidal rule). Numerical tests for this procedure can be found in Torres-Forné et al. (2018).

Given that we are integrating a system of six ODEs, we have to provide six boundary conditions. Since we are using a staggered grid, our first integration point is not at $r = 0$. This implies that we have to provide non-zero values for all quantities at this point to perform the integration. Due to the regularity conditions seen in Section 2.3, it is sufficient to fix the value of three quantities, η_r , $\delta\hat{Q}$ and $\delta\hat{\psi}$, and the remaining three are automatically known.

The value of η_r can be set arbitrarily and it fixes the amplitude of the eigenfunction. The two additional variables have to be fixed such that the boundary conditions at the shock location, Eqs. (54) and (55), are fulfilled. To ensure this, we use a shooting method, which consists in varying the values of $\delta\hat{Q}$ and $\delta\hat{\psi}$ at the innermost radial point, integrating outwards, and checking whether the boundary conditions are fulfilled. We perform this iteration using a vectorial

Newton-Raphson method, where the derivatives of the Jacobian are computed numerically using a stencil of the size given by the previous step.

We also compute the eigenmodes using an alternative numerical method. The description of this method and the comparison with the first one can be found in Appendix B. In all tested cases, the differences in the eigenfrequencies between both methods were smaller than 0.1%. In some cases (for very low frequencies) the alternative method shows numerical convergence problems that are not found in the first method. Therefore, all results presented in this paper have been obtained using the first method, which is more robust.

The computation of \mathcal{G} , defined in Eq. (13), involves some degree of arbitrariness because it can be computed either from the gradient of the pressure ($\mathcal{G}_P \equiv \partial_r P / \rho h$) or from the gradient of the lapse ($\mathcal{G}_\alpha \equiv -\partial_r \ln \alpha$). Unless stated otherwise we use $\mathcal{G} = \mathcal{G}_P$. We explore the effect of the definition of \mathcal{G} in the eigenmode calculation in Section 4.1.

3.3 Eigenmode classification

The procedure we have just described allows us to compute the eigenvalues, along with their corresponding eigenfunctions, for a set of time slices of a simulation. However, it does not provide information about the nature of each eigenmode. Stellar oscillations can be classified according to the dominant restoring force giving rise to them, either pressure (p -modes) or buoyancy (g -modes). The local quantities determining the character of the modes are the Lamb frequency, \mathcal{L} , and the Brunt-Väisälä frequency, \mathcal{N} . Pressure supported (sound) waves with frequency σ are possible in regions of the star in which $\sigma^2 > \mathcal{L}^2, \mathcal{N}^2$, while buoyancy supported (gravity) waves are possible in regions with $\sigma^2 < \mathcal{L}^2, \mathcal{N}^2$ (see e.g. Cox 1980). The regions of the star where σ^2 is between \mathcal{L}^2 and \mathcal{N}^2 are evanescent and no waves propagate in this region. Note that if $\mathcal{N}^2 < 0$ gravity waves are not possible because the system is convectively unstable. Using these properties several classification procedures are possible, which have been developed in the context of asteroseismology (see e.g. Unno et al. 1979; Cox 1980).

3.3.1 Cowling classification

The first classification of non-radial oscillation modes of spherical stars was introduced by Cowling (1941)². For stars with monotonically decreasing \mathcal{L}^2 (note that it is proportional to r^{-2}) and monotonically increasing \mathcal{N}^2 (typical of simple stratified equilibrium models; see e.g. Cox 1980) there is a critical frequency above which only sound waves can propagate and below which only gravity waves are possible. This allows for a very simple classification purely based in the number of nodes of the radial part of the eigenfunction, η_r . The mode with zero radial nodes is the fundamental mode or f-mode, denoted as ${}^l f$. Modes with higher frequencies are p -modes, denoted as ${}^l p_n$, with increasing number

² We warn the reader not to confuse the Cowling approximation (static space-time approximation) and the Cowling classification procedure of modes, both introduced in Cowling (1941).

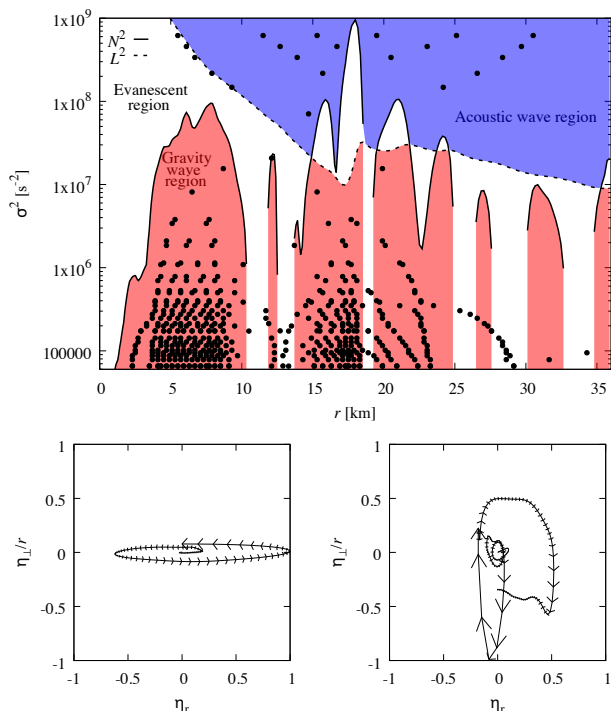


Figure 2. Propagation and phase diagrams for $l = 2$ modes in model 35OC at 1.3 s post bounce. *Upper panel:* Propagation diagram showing the radial profile of the Brunt-Väisälä frequency (N^2 , solid black line) and the Lamb frequency (L^2 , dashed black line). Note that in some regions $N^2 < 0$ and no gravity waves are possible. Colours indicate the acoustic wave region (blue, $\sigma^2 > N^2, L^2$), the gravity wave region (red, $\sigma^2 < N^2, L^2$), and the evanescent region (white). Black dots indicate the location of the radial nodes of η_r for all the eigenmodes found at different σ . *Lower panels:* phase diagram for two eigenmodes at 3542 Hz ($\sigma^2 = 5.0 \times 10^8 \text{ s}^{-2}$) corresponding to a p-mode (lower left) and at 237.8 Hz ($\sigma^2 = 2.2 \times 10^6 \text{ s}^{-2}$) corresponding to a g-mode (lower right). Arrows indicate the direction of increasing r . The trajectory rotates clockwise in gravity wave regions and counter-clockwise in sound wave regions.

of nodes, n , for increasing frequency. In a similar way, g-modes, denoted as ${}^l g_n$, have frequencies lower than the f-mode and have increasing number of nodes, n , for decreasing frequency. A variant of this classification has been used in Torres-Forné et al. (2018). In that work, h-modes (hybrid) were introduced to distinguish modes above or below the f-mode, but with the same number of nodes. The upper panels of Fig. 3 below show the eigenmodes classified according to the Cowling classification (variant described in Torres-Forné et al. (2018)).

Although it can serve as a guide, the Cowling classification does not work properly in every case, in particular in those cases with no critical frequency. In those cases, it may happen that, for a given frequency, there are regions of the star supporting gravity waves at the same time as other regions support sound waves, sometimes separated by evanescent regions (see upper panel of Fig. 2). In those cases the ordering devised by Cowling may not apply and one has to rely upon a more general procedure (see Unno et al. 1979; Cox 1980, for a deeper discussion). An indication that this is indeed a problem in our models is the necessity of intro-

ducing h-modes in the classification. As we show below, this is an artefact of the classification scheme.

3.3.2 ESO classification

To overcome the problems of the Cowling classification Eckart (1960), Scuflaire (1974) and Osaki (1975) developed a classification scheme (ESO scheme, hereafter) based not only on the number of radial nodes, but also in the character of each node. Using the radius r as a parameter, each mode can be plotted in the η_r vs η_\perp phase diagram. Nodes in the radial direction correspond to crossings of the “x” axis (η_r). For g-modes, the trajectory of the mode in the phase diagram (parametrised with r) is clockwise (see lower right panel of Fig. 2, for an example), while p-modes have counter-clockwise trajectories (lower left panel of Fig. 2). For frequencies in regions supporting gravity waves and regions supporting sound waves, the trajectory in the phase diagram is clockwise and counter-clockwise in each of the regions. The ESO scheme is based on the number of clockwise turns minus the number of counter-clockwise turns in the phase diagram, n_{ESO} . For $n_{\text{ESO}} > 0$ the mode is predominantly a g-mode and it is classified as a ${}^l g_n$, with $n = n_{\text{ESO}}$. For $n_{\text{ESO}} < 0$ the mode is predominantly a p-mode and it is classified as a ${}^l p_n$ with $n = -n_{\text{ESO}}$. The mode with $n_{\text{ESO}} = 0$ is the f-mode. The second row of panels of Fig 3 shows the ESO classification method applied to our models.

The ESO scheme significantly improves the classification of the modes, although it still has some drawbacks. One of the problems is the existence of trapped modes. If one looks at the propagation diagram in the upper panel of Fig. 2, at mid-range frequencies ($\sigma^2 \sim 5 \times 10^8 \text{ s}^{-2}$) there is a region within 10 km from the center where only gravity waves are possible and at the same time sound waves are only possible above ~ 12 km. Both regions are disconnected by an evanescent region, so in principle it is possible to have trapped modes inside each of the two regions, corresponding to a g-mode and a p-mode, respectively, at the same (or similar) frequencies. In practice these two modes interact with each other channeling through the evanescent region and giving raise to a more complex mode which is a hybridisation of both. This effect can be observed in both of our models, when looking at the time evolution of the eigenfrequencies (Fig. 3, see ESO classification). As the frequency of any two modes becomes similar the phenomenon of the avoided crossing appears.

To illustrate the phenomenon of the avoided crossing, let us consider the ${}^2 f$ and ${}^2 g_1$ modes at ~ 750 ms in the model s20. According to the ESO classification scheme, the ${}^2 f$ mode has higher frequency than the ${}^2 g_1$ during the avoided crossing (see left panel in the second row of Fig 3). This produces an abrupt change of frequency near 750 ms, which may appear as an artefact of the classification scheme (it would look more natural if they crossed). Fig. 4 shows η_r for these two modes before (610 ms), during (757 ms) and after (860 ms) the crossing. Before the crossing (left panel) the ${}^2 f$ mode appears more concentrated in the outer parts of the system (outside the PNS), while the ${}^2 g_1$ mode extends to the interior of the PNS. However, after the crossing (right panel) the situation is reversed, appearing as if the ESO scheme would have misclassified the modes. During the avoided crossing, both modes hybridise (middle panel) and

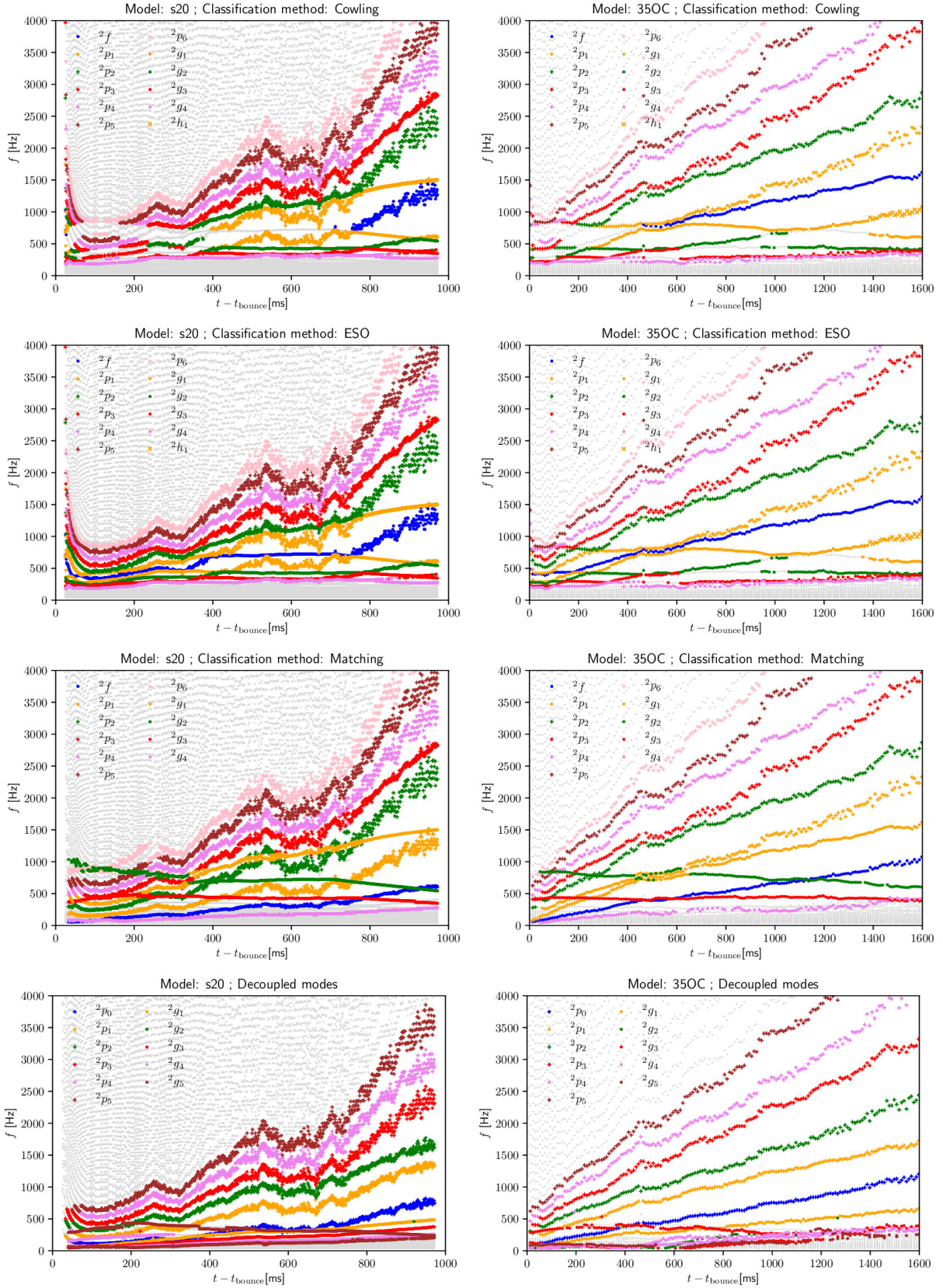


Figure 3. Evolution of the eigenfrequencies for $l = 2$ for models s20 (left panels) and 350C (right panels) using the Cowling (upper panels), ESO (second row) and matching (third row) classification procedures. The bottom panels correspond to the decoupled computation of the modes. A selection of the classified modes (indicated in the legends) is plotted in colours and the rest of the modes are plotted in grey.

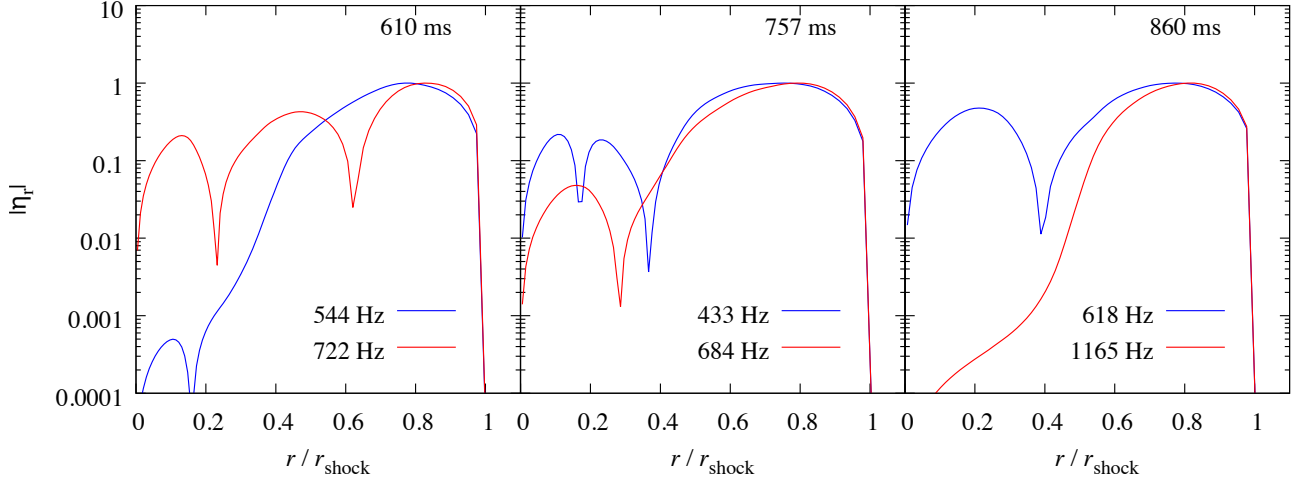


Figure 4. Amplitude of the radial eigenfunction for the fundamental $l = 2$ $2f$ mode (blue) and the $2g_1$ g-mode (red) for the s20 model, classified according to the ESO scheme, around the time of the avoided crossing ($t - t_{\text{bounce}} \sim 750$ ms).

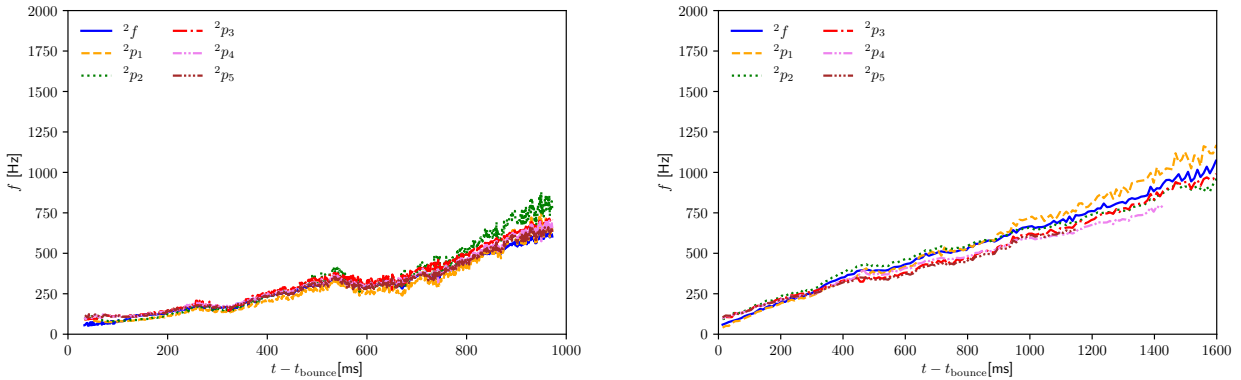


Figure 5. Evolution of the frequencies of the $2p_n$ modes divided by $n + 1$ compared to the $2f$ mode, both for the s20 model (left) and the 35OC model (right).

are actually quite similar (except for the number of nodes), which is the result of the process described in the previous paragraph. This phenomenon is well known in asteroseismology, and not a numerical artefact of the ESO scheme. However, the ESO classification scheme poses a problem for the purpose of this work. Our goal is to learn how the eigenmodes behave during the post-bounce evolution to try to devise ways, in the future, to infer properties of the PNS based on GW observations. For this purpose it is crucial to characterize the GW features seen in spectrograms (mostly described as raising archs) and classify together modes with similar features (e.g. localised in the same part of the PNS) which are likely to be excited with similar energy and produce a similar GW output, during the post-bounce evolution. For this reason we need a method that is based in the similarity of the eigenfunctions and not in the number of nodes.

3.3.3 Matching classification

In this work, we present a new classification procedure which is not based in the number of nodes but in the shape of the eigenfunctions. Our procedure traces the eigenmodes in time by finding the best match between the shape of the eigenfunction in each time step and those from the previous time steps. We have found that this procedure works best when the matching is done backwards in time. The details of the matching algorithm can be found in Appendix C. Hereafter, we refer to this algorithm as the *matching classification*. Note that the algorithm does not give a proper classification in the sense that it does not tell g-modes from p-modes or the f-mode, it just groups modes at different times in groups according to similarity. To tag each mode sequence with an appropriate class we use as a reference the ESO classification at the last time available, with some additional modifications that we discuss next. The third row panel of Fig. 3 shows the classification results for the matching scheme. With the new procedure the behaviour in time of the eigenmodes is smoother and there are mode crossings at places where avoided crossings appeared with the previ-

ous two classification methods. In particular, in the crossing of modes in the s20 model discussed above, the shapes are preserved (modes are swapped with respect to Fig. 4), but the number of nodes changes. This feature is consistent for all modes and a more detailed analysis of the eigenmode shape is given in the next section. Note that in the new classification scheme, the number of nodes indicated in the name of the class (e.g. 2g_1 , one node) is not indicative of the actual number of nodes. This new mode classification method is not perfect, and some modes are still clearly misclassified (specially high order g-modes). However, for low order modes it gives consistent results. We will argue in the next sections that these modes are the most relevant for GW emission, and therefore our classification should be sufficient for this purpose.

To better understand the classification of the modes we solve the eigenvalue problem decoupling p-modes and g-modes. This can be achieved by setting $\mathcal{B} = 0$ or $c_s^2 \rightarrow \infty$, respectively, as described in Torres-Forné et al. (2018). The two lower panels of Fig. 3 shows the decoupled modes in these limits. We use this information to retag some of the modes classified by the matching algorithm to better match the identification made in the decoupled computation. This result also confirms that the avoided crossings seen in the Cowling and ESO classifications are related to crossings of the decoupled modes and therefore our matching algorithm is unveiling these crossings properly. We note that many of the decoupled modes also differ significantly in frequency with respect to the corresponding modes computed with the full system. In particular, g-modes tend to have higher frequencies in the full system, likely due to the presence of acoustic wave regions where those waves can propagate significantly faster than gravity waves.

One of the consequences of the matching classification scheme is that it renders unnecessary to introduce h-modes to classify all modes. For example, what was misclassified as an 2h_1 mode in the Cowling and ESO classification for the 35OC model, as well as in Torres-Forné et al. (2018), is actually classified as the f-mode with the new scheme and all p-modes have a value of n displaced in one unit with respect to our previous classifications. A more definitive proof that our matching procedure classifies correctly the f-mode and the p-modes is that the frequency of the 2p_n modes is approximately an integer number ($n+1$) the frequency of the f-mode (See Fig. 5). This relation is significantly better than the one found in Torres-Forné et al. (2018), which misclassified the f-mode. It also clarifies the intriguing feature found in Torres-Forné et al. (2018), of a h-mode with a frequency which was an integer fraction of the higher order p-modes. This mode simply was the f-mode.

Finally, we would like to indicate that there are other classification schemes in the literature (e.g. Takata 2012), which tried to overcome the limitations of the ESO scheme using different approaches. How these classification schemes compare to our approach is something that could be explored in future work.

3.4 Eigenmode morphology

Figures 6 to 8 show the time evolution of the Newtonian eigenmode energy density, defined by Eq. (59), for a selection of modes classified in three groups according to their shape:

- *f-mode and p-modes*: Fig. 6 shows a selection of modes (2f , 2p_1 , 2p_2 , 2p_3) with a relatively large amount of energy density outside the PNS. These modes are basically trapped sound waves in the region between the PNS surface and the shock. However, due to the complex hybridisation process mentioned above, they also couple with regions deep in the PNS interior, specially at frequencies where mode crossings appear. For higher values of n the number of nodes (here appearing as deeps in \mathcal{E}) increases as expected for higher order overtones of the f-mode. All these modes have in common that their frequencies increase in time (except for some periods in the s20 model) and that the frequencies are integer multiples of the f-mode frequency.

- *Core g-modes*: Fig. 7 collects modes with the largest amplitude inside the PNS (2g_1 , 2g_2 and 2g_3). While lower n modes are more extended over the whole PNS, higher order modes become more concentrated in the inner core region. These modes correspond to g-modes associated with the stable region in the innermost part of the PNS (see Fig. 9). The frequency evolution of these modes is similar for both models. While the 2g_1 mode shows an almost monotonic increase in frequency, higher order overtones (2g_2 and 2g_3) decrease their frequency with time.

- *Surface g-modes*: Fig. 8 collects modes with the largest amplitude at the surface of the PNS (e.g. 2g_4). These modes result of the excitation of the buoyantly stable layer ($\mathcal{N}^2 > 0$) at the surface of the PNS (see Fig. 9). These modes show an almost monotonically increase of their frequency during their evolution, although they are confined to low frequencies (< 250 Hz).

This interpretation is consistent with previous analysis (albeit more simplified) of the PNS structure (Cerdá-Durán et al. 2013; Andresen et al. 2017), which showed that the features observed in the GW spectrograms could be related to g-modes in two different regions (surface and inner core).

4 COMPARISON WITH SIMULATIONS

4.1 GW spectrograms

In this section we compare the eigenmode frequencies obtained applying the linear analysis to the spherical background with the GW frequencies computed in the numerical simulations, result of the multidimensional dynamics of the model. Fig. 10 shows the GW signal (upper panels), the corresponding spectrograms (middle panels) and the spectrograms with a selection of modes over-plotted (lower panels). As mentioned before, there is some uncertainty in the definition of \mathcal{G} . To gauge the difference between using \mathcal{G}_P and \mathcal{G}_α , we plot in all cases the modes computed in both ways. The range between both options gives a measure of the error introduced by the definition of \mathcal{G} .

For the non-rotating s20 model (left panels), both calculations lay on top of each other. This is a strong indication that the assumption of hydrostatic equilibrium inside the shock is indeed a very good approximation. However, in the rapidly-rotating model 35OC (right panels), there is a significant difference between both definitions of \mathcal{G} in many of the models (solid lines correspond to \mathcal{G}_P and dashed lines to \mathcal{G}_α). The difference may be due to the fact that we are neglecting rotation in our linear analysis. In fact, centrifug-

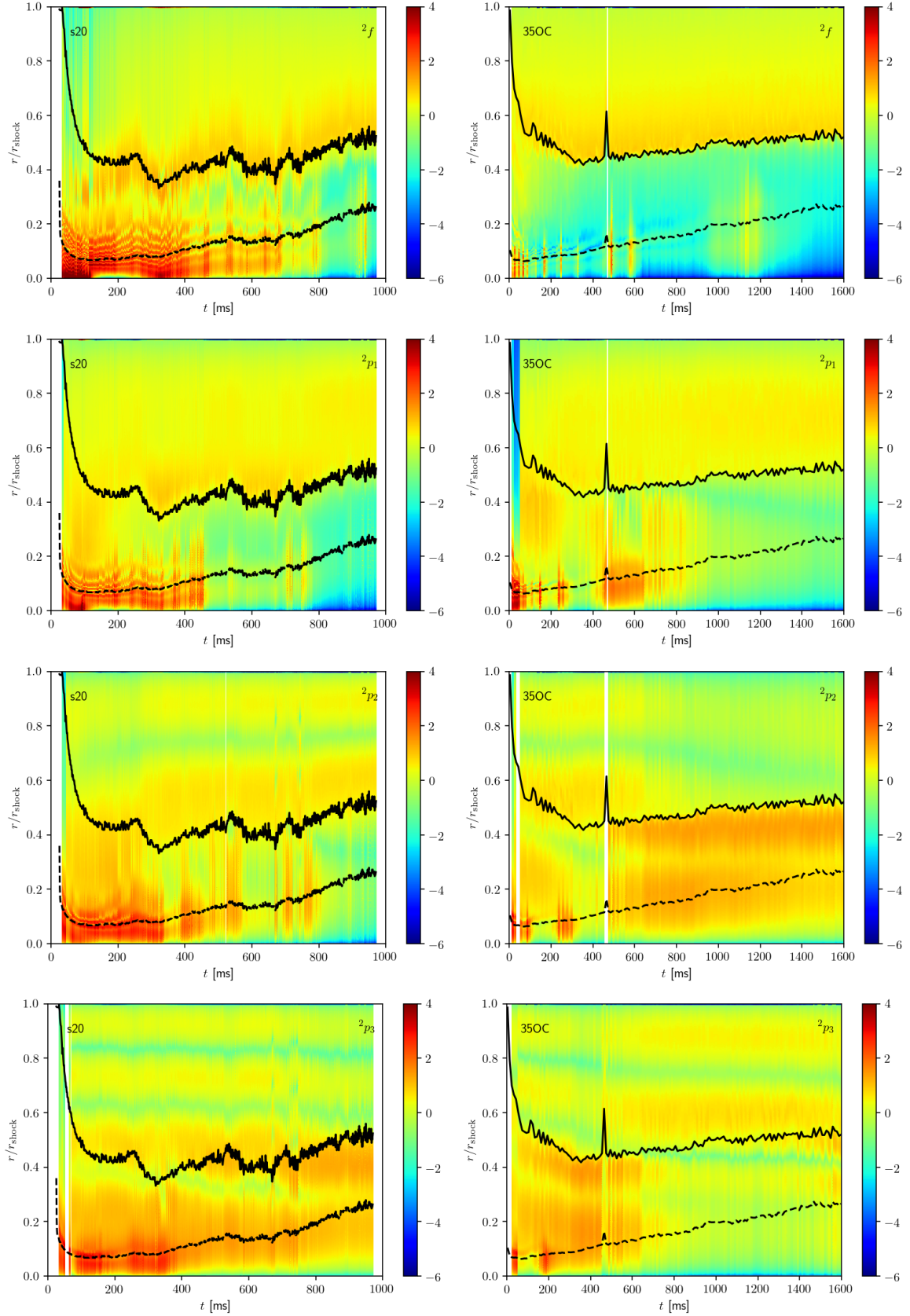


Figure 6. Time evolution of the radial profile of the logarithm of the energy density, $\mathcal{E}(r)$, for a selection of modes classified as p-modes and the f-mode for models s20 (left panels) and 35OC (right panels). The solid black line indicates the position of the PNS surface and the dashed black line the surface of the inner core. The radius is normalised to the shock location. White stripes indicate times in which no modes were found.

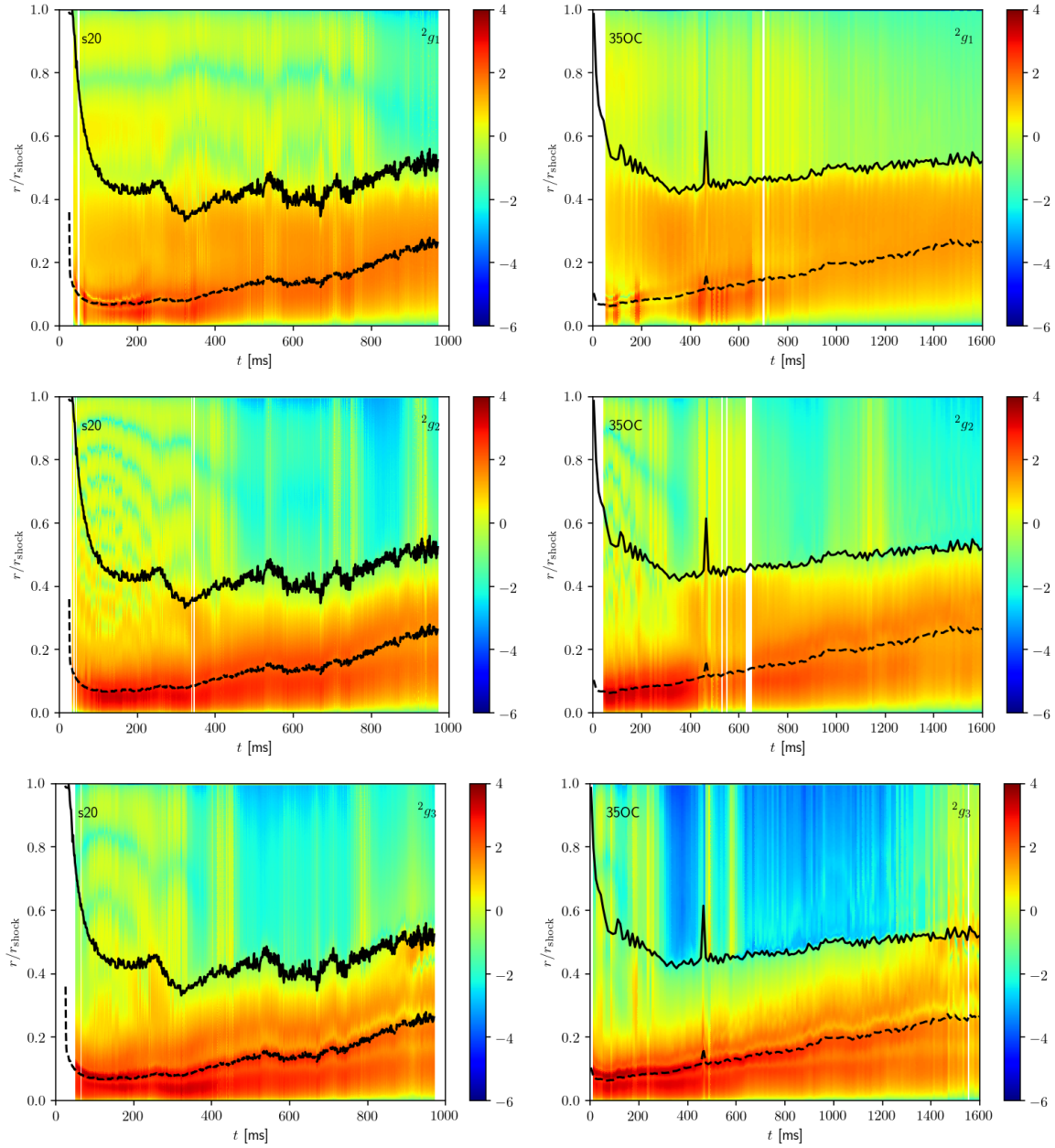


Figure 7. Same as Fig. 6, but for a selection of modes classified as core g-modes.

gal forces play an important role in the equilibrium for this model and, thus, this result is not a surprise. What is reassuring (and somewhat striking) is that, even using a non-rotating analysis, the features observed in the spectrogram lay between our two possibilities for the eigenmode computation.

In general, for both models (see lower panels of Fig. 10 there is a clear agreement of a selection of modes with the features in the spectrograms, which is a clear indication that these modes are responsible for the computed GW emission. In model s20 (bottom left panel) the agreement for modes 2g_1 and 2g_2 is remarkable with some hints of the presence of the 2f mode. Although p-modes are not clearly visible, some excess power above the 2g_1 mode may be an indication of their presence. In model 35OC (bottom right panel), all main

features can be explained with a few modes. Most of them match well the spectrogram within the error produced by the definition of \mathcal{G} . The only exception is the 2f mode, whose evolution runs in parallel to the spectrogram feature but with higher frequency. The main features can be explained by the 2g_1 mode and the 2p_1 mode. The f-mode and all p-modes up to order 5 are also clearly visible, albeit with lower amplitudes. We note in particular that our computation of the $l = 0$ mode is able to reproduce the characteristic feature of this mode close to black hole formation, namely that its frequency goes to zero at the onset of instability (Cerdá-Durán et al. 2013), as predicted by Chandrasekhar (1964).

In addition to estimating the effect of the definition of \mathcal{G} in our mode comparison, we also test its effect in the expression for the Brunt-Väisälä frequency. In this work we

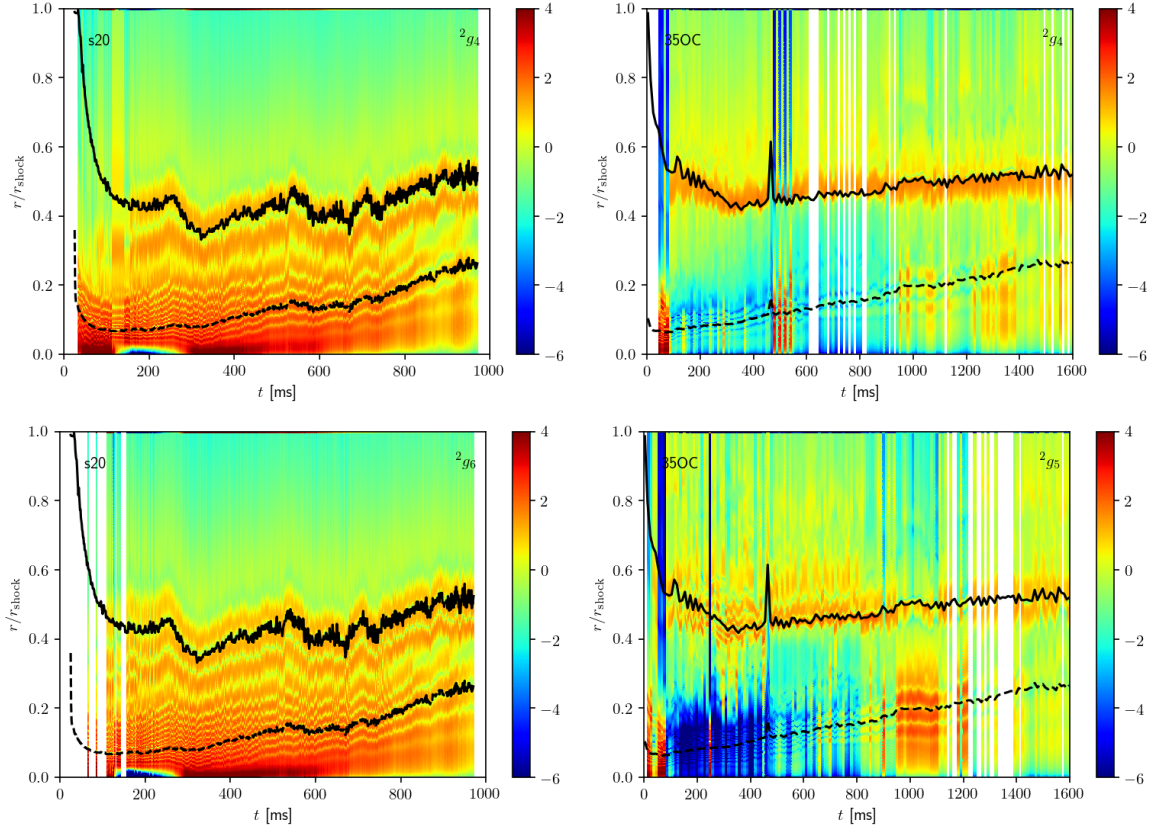


Figure 8. Same as Fig. 6, but for a selection of modes classified as surface g-modes. Note that in the model 35OC some modes have been misclassified by our algorithm and appear as sharp transitions.

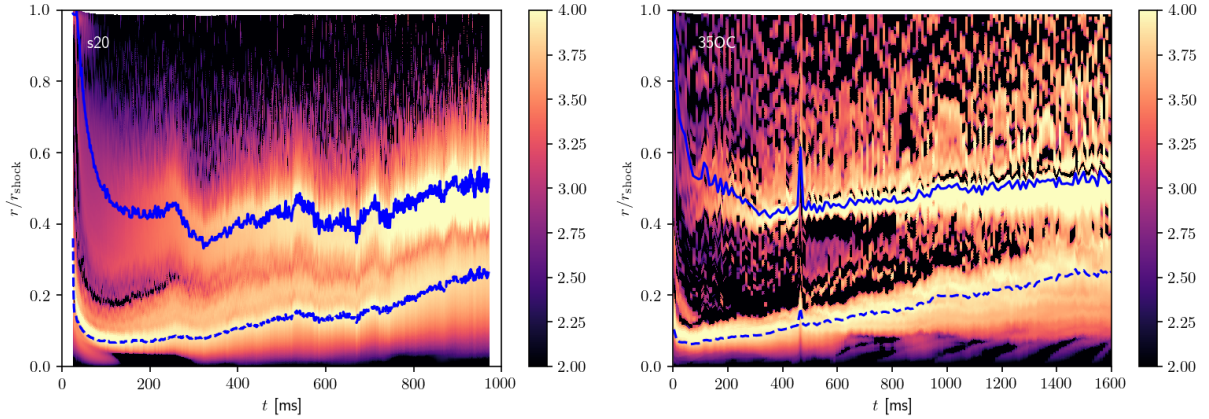


Figure 9. Logarithm of the Brunt-Väisälä frequency, \mathcal{N} , for positive values of \mathcal{N}^2 , i.e. regions stable against convection. Convectively unstable regions ($\mathcal{N}^2 < 0$) are plotted in black. The blue black line indicates the position of the PNS surface and the dashed blue line the surface of the inner core. The radius is normalised to the shock location.

first perform an angular average of the simulation data and then we compute the Brunt-Väisälä frequency as $\mathcal{N}^2 = \mathcal{G}\mathcal{B}$, being \mathcal{G} and \mathcal{B} the radial component of the vectors \mathcal{G}_i and \mathcal{B}_i . Alternatively one can compute $\mathcal{N}^2 = \mathcal{G}_i\mathcal{B}^i$, on the 2D grid of the simulation and then perform the angular average to obtain 1D profiles of \mathcal{N}^2 . For the fast rotating case, the second procedure takes into account the non-radial components of \mathcal{G}_i and \mathcal{B}_i , which are otherwise neglected in the first procedure. We have computed the eigenmodes using

both definitions and the differences in the computed eigenfrequencies do not differ by more than 1%.

Regarding gravity, this work improves over previous work that considered no metric perturbations (Cowing, Torres-Forné et al. 2018) and only perturbations of the lapse function (Morozova et al. 2018). To compare with different approaches for the metric perturbations we have performed our analysis in Cowling and considering only perturbations of $\delta\hat{Q}$, which corresponds to including only perturbations of

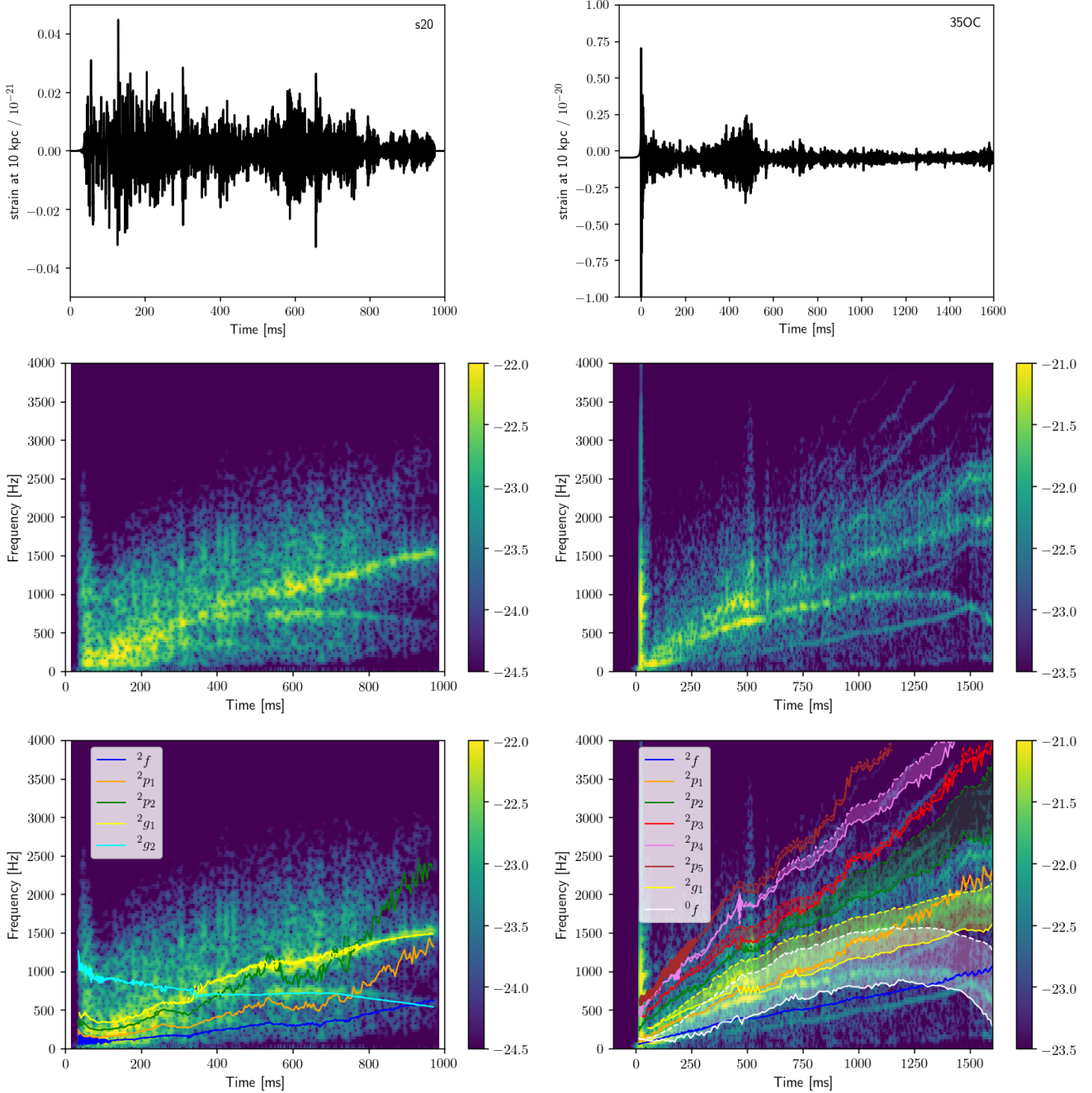


Figure 10. This figure shows the GW signal (upper panels), the corresponding spectrograms (middle panels), and the spectrograms with a selection of modes over-plotted (lower panels) for models s20 (left) and 35OC (right). Solid lines and dashed lines are used to indicate that the calculations were made using \mathcal{G}_P and \mathcal{G}_α , respectively. Note that for model s20 those two lines overlap.

the lapse function. Fig. 11 compares the three approaches. In general, the differences among them increase at later times. This is because the PNS becomes gradually more compact and GR effects become more relevant. Note in particular the 2g_1 mode for the s20 model (yellow lines in the left panel), in which only the approach followed in the present work is able to reproduce the features observed in the spectrogram. For the rotating model 35OC, this is more difficult to discuss, because the differences with respect to the spectrogram are also strongly influenced by rotation. However, it is worth

highlighting that our approach is the only capable of reproducing the turning down of the 0f mode at the onset of black hole formation, while the other two approaches give qualitatively different behaviors. Therefore, we conclude that our approach is necessary whenever high accuracy in the eigenmode calculations is needed, specially close to black hole formation. Moreover, the high accuracy obtained in model s20 provides convincing evidence that perturbations of the shift vector, neglected in our analysis, are not important, at least for slowly-rotating systems.

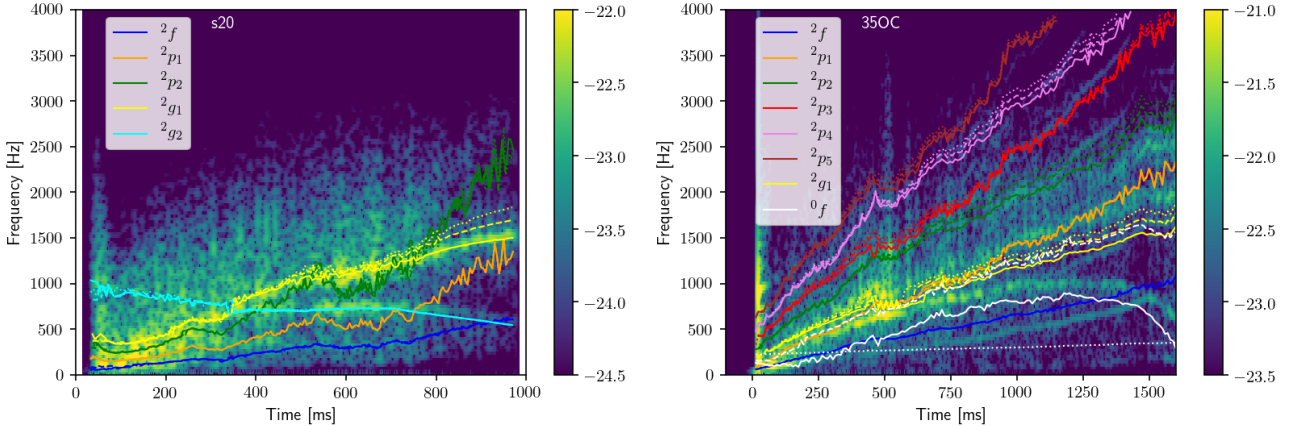


Figure 11. Spectrograms with a selection of modes over-plotted using spacetime perturbations (solid lines), only metric perturbations of $\delta\hat{Q}$ (dashed lines), and no metric perturbations (Cowling, dotted lines), for models s20 (left) and 35OC (right).

4.2 GW efficiency and mode energy

To understand which modes are more efficient GW emitters, we compute the GW efficiency (see Eq. (65)) for $l = 2$ and $l = 0$ modes. This calculation provides an estimation of the fraction of the energy stored in an eigenmode that is emitted per oscillation cycle. Model s20 is non rotating, so the $l = 0$ mode will not contribute to the GW signal. Model 35OC corresponds to a rapidly rotating progenitor, which results in a PNS with a central period of about 1.5 ms at bounce. The PNS is considerably deformed, with a polar-to-equatorial radius ratio of 0.64 after bounce and the GW amplitude is expected to be significantly affected by rotation (see Section 2.4.2). We use Eq. (87) to estimate the quadrupolar moment needed for the computation of the GW efficiency. In our numerical simulation the ratio r_e/r_p ranges from ~ 1.25 (in the PNS core) to ~ 1.7 (at the PNS surface), which correspond to ellipticities in the range $e \sim 0.6 - 0.8$. The pre-factor to the integral of Eq. (87) is in the interval $-0.06 - 0.14$ for our ellipticity range. This means that, for similar eigenfunction structure and mode energy, the $l = 0$ modes are expected to emit GWs with an amplitude of about 10% the amplitude of the $l = 2$ modes.

Fig. 12 shows the GW efficiency for both models. Similarly to the results of Torres-Forné et al. (2018), the efficiency grows with the frequency, with the p-modes being in general more efficient than the g-modes. This happens because the GW efficiency approximately scales with σ^3 . The implication is that to see low-frequency modes in the spectrogram one needs considerably large energy in those modes. In both models the most visible features correspond to the lowest order modes, while high order p-modes are only observed in the 35OC model, likely related to the SASI activity (see the related discussion in Section 5). In neither model high order g-modes are observed, the highest order mode observed being the 2g_2 of the s20 model.

Given that we know the complete eigenmode structure, we can use the spectrogram to estimate the energy stored in each mode and try to validate the previous claims. To this end, we extract the amplitude of the GW emission at some intervals along the main features of the spectrogram. Then, we rescale the amplitude of the eigenmodes so that their

GW emission amplitude computed with Eq. (64) matches the value obtained from the spectrogram. The results of this calculation for model s20 are shown in the upper panel of Fig. 13. The modes which correspond to the main features on the spectrogram (Fig. 10 middle left panel) are the 2g_1 and the 2g_2 . The highest power in GW corresponds to the 2g_1 mode, while the other mode presents a slightly less amplitude. However, the energy stored in each mode (Fig. 13) exhibits the opposite behaviour. This is due to the GW efficiency (Fig. 12 upper panel). As the efficiency of the 2g_2 mode is much lower than that of the 2g_1 mode, the corresponding energy should be larger to radiate a similar energy in GW. In the case of model 35OC (Fig. 13 lower panel), we have analyzed the four modes which show the most clear trace in the spectrogram (Fig. 10 middle right panel). The energies are ordered as expected. The two fundamental modes, 0f and 2f , have the largest energies because their GW amplitude are large (their traces on the spectrogram are clearly visible) but their efficiencies are low.

5 SUMMARY AND DISCUSSION

In this work we have developed a numerical procedure to solve the eigenvalue problem of hydrodynamic and metric perturbations of a spherically symmetric self-gravitating system in general relativity. We have applied this method to compute the oscillation frequencies of the PNS-shock system formed during a core-collapse supernova explosion. Those frequencies have been compared to the time-frequency patterns observed in the GW templates from two CCSN numerical simulations. This work is an extension of our previous investigation (Torres-Forné et al. 2018) and brings forth significant improvements with respect to previous results. The numerical routines developed and used in this work to solve the eigenvalue problem are available at the GREAT library (General Relativistic Eigenmode Analysis Tool) that we have released as open source (<https://www.uv.es/cerdupa/codes/GREAT/>).

The main results of this work can be summarized as follows:

- We have incorporated perturbations of the lapse func-

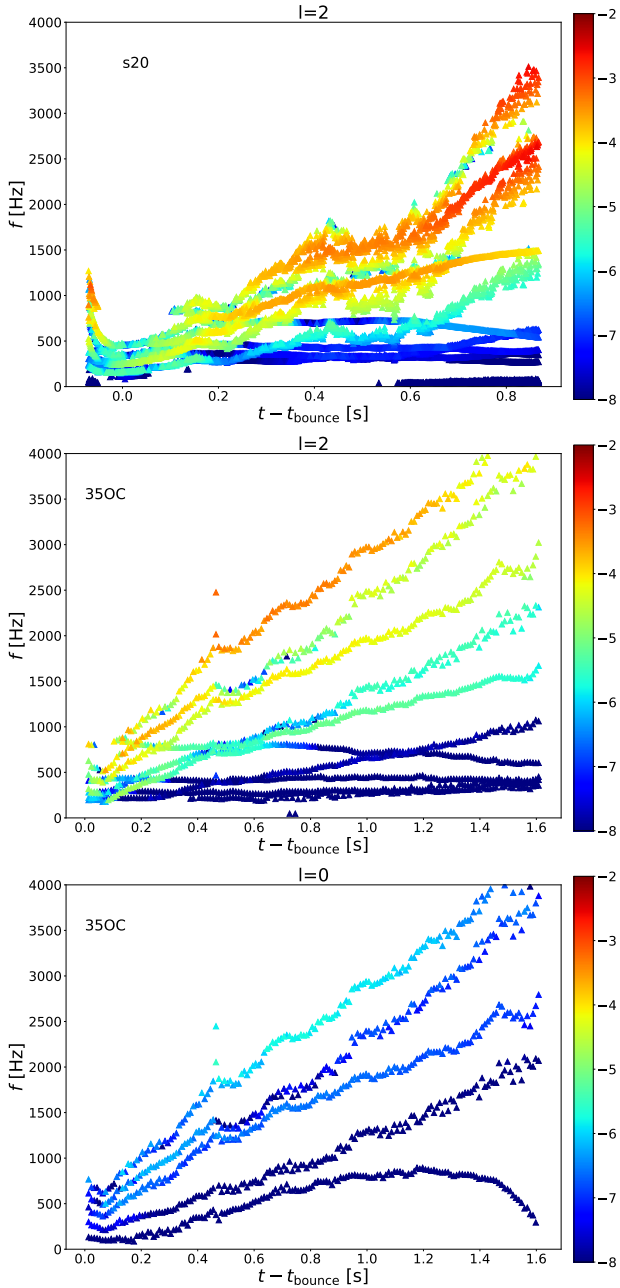


Figure 12. GW efficiency for the $l = 2$ modes in model s20 (upper panel) and for the $l = 2$ and $l = 0$ modes in model 35OC (middle panel and lower panel, respectively).

tion and of the conformal factor, improving the approach of Torres-Forné et al. (2018), based on the Cowling approximation, and of Morozova et al. (2018), which considered only perturbations of the lapse function. Our results show that it is necessary to consider both kinds of perturbations to accurately reproduce the $l = 2$ modes in the GW spectrograms. Regarding $l = 0$ modes, our approach is the only one able to trace the qualitative time-frequency behaviour of the 0f mode, for which the frequency decreases towards zero at the onset of black hole formation. This mode is of particular importance because it indicates the formation of a black

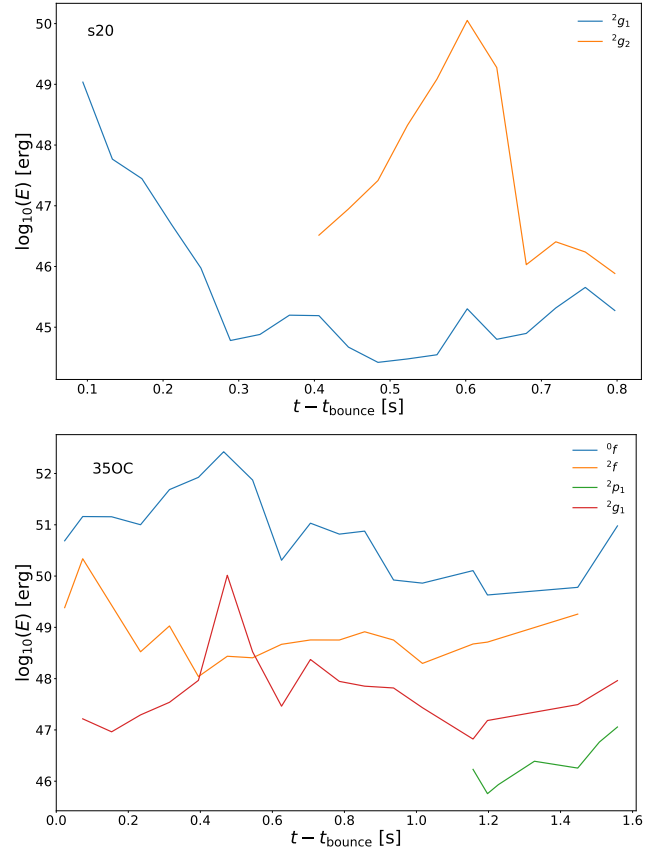


Figure 13. Energy of the principal emission modes in logarithmic scale for $l = 2$ modes in model s20 (upper panel) and for $l = 2$ and $l = 0$ modes in model 35OC (lower panel).

hole and could be observed for rapidly rotating cores. Our approach has not accounted for perturbations of the shift vector. However, given the accuracy of our results, incorporating those perturbations does not seem necessary, at least for non-rotating models.

- For our nonrotating model s20, we have found an excellent agreement between the features observed in the spectrogram and the computed eigenmodes. For rapidly rotating cores, the assumed spherically-symmetric background is not valid and the results are only qualitatively similar to the GW signal, due to the effect of centrifugal forces, not considered in our analysis.

- In both CCSN models, s20 and 35OC, the 2g_1 mode has been identified as the main contributor to the GW signal. The 2f mode is also visible in the two models, along with a few overtones. Furthermore, we have estimated the eigenmode energy according to the amplitude of the GW signal for each mode. This analysis confirms that most of the energy is stored in the lowest order eigenmodes.

- We have developed a formalism to estimate the contribution of quasi-radial modes ($l = 0$) to the quadrupolar component of the GW signal in the case of deformed backgrounds. This is of particular importance for rapidly rotating cores in which the PNS is deformed by the effect of centrifugal forces.

- Our improved analysis has been possible thanks to a

newly developed matching classification scheme, that allows to classify the eigenmodes in p-, g- and f-modes, in a more accurate way as the preceding methods used in [Torres-Forné et al. \(2018\)](#).

Despite our investigation has been limited to only two numerical models, some conclusions about the mechanism producing GWs during the collapse of massive stars can be extracted from this work, in particular when comparing with previous results in the literature. The presence of a clear pattern of rising frequencies in the GW spectrograms of the post-bounce evolution of PNSs has been observed in a number of works ([Murphy et al. 2009](#); [Müller et al. 2013](#); [Cerdá-Durán et al. 2013](#); [Yakunin et al. 2015](#); [Kuroda et al. 2016](#); [Andresen et al. 2017](#)). In all these works, this raising pattern was attributed to g-modes of the PNS. Our work shows that this main feature is probably the 2g_1 mode, i.e. the lowest order g-mode, associated with the buoyantly stable region in the innermost part of the PNS, and not to its surface. Although surface g-modes are possible according to our analysis, we do not see their correspondence in the GW spectrograms of the two models computed. This is very likely due to the low GW efficiency of these modes, which displace a much smaller amount of matter when compared with the core g-modes.

Some works in the literature ([Cerdá-Durán et al. 2013](#); [Kuroda et al. 2016](#); [Andresen et al. 2017](#)) have related the presence of a low frequency (~ 100 Hz) component in the GW signal to the characteristic frequency of the SASI. In this work, however, we have identified the mode observed in [Cerdá-Durán et al. \(2013\)](#) as the fundamental 2f mode, and we suspect a similar result will hold for the results of [Kuroda et al. \(2016\)](#) and [Andresen et al. \(2017\)](#). The fundamental mode (and also higher order p-modes) seems to be excited in cases with strong SASI activity. [Cerdá-Durán et al. \(2013\)](#) showed that these features observed in the GW spectrogram match perfectly with the features observed in the spectrogram of the time evolution of the shock, i.e. the shock oscillates with frequencies matching the p-modes. It is not completely clear why this is the case (see discussion in [Cerdá-Durán et al. 2013](#)). In principle, in the presence of the SASI the shock oscillates with frequencies corresponding to the unstable modes of the advective-acoustic cycle coupling the shock and the PNS surface ([Foglizzo 2002](#); [Foglizzo et al. 2007](#)), which should not coincide with the frequencies of the purely acoustic cycle (p-modes in our case). We are not sure if the matching of the frequencies observed in our analysis is generic or if it is a particular feature of the 35OC model (e.g. a resonance). The analysis presented in this work can be applied to other multidimensional simulations presenting signatures of SASI to try to better understand the relationship between p-modes and SASI.

Our clear identification of the 2g_1 and 2f modes is of great importance to devise strategies to infer PNS properties from a possible GW observation of a nearby SN (or BH formation) event. It follows from our work that most of the future efforts must focus in these two particular modes, in order to learn how they depend on the properties of the PNS. This will also allow to develop data analysis methods aimed at detecting this kind of GW signals buried in detector noise.

Our analysis may also simplify the GW templates from CCSNe, since most of the information (the time-frequency

behaviour) encodes the general evolution of the PNS, and not the particular non-linear perturbations, which are to a large degree stochastic. Some of the information cannot be extracted from our analysis, most notably the energy stored in each of the eigenmodes, which does not allow us to provide complete templates of CCSNe. For this we still will have to rely on sophisticated core-collapse simulations. One of the main questions that has to be addressed is what is the evolution of the energy content of each eigenmode. The results presented here are only for two 2D simulations, but the energy distribution may change significantly in 3D simulations or in simulations accounting for more sophisticated microphysics or neutrino transport.

Finally, we note that the results presented in this work strongly rely in our new eigenmode classification algorithm. Previous results by [Cerdá-Durán et al. \(2013\)](#) suffered from serious misclassification issues. In particular, the so-called SASI mode was not classified as the fundamental mode, which arose confusion to explain why it was an integer division of the higher order modes. This is however explained naturally with its identification as an f-mode, possible with the new matching classification scheme. This method is not completely automatic and requires some degree of manual intervention. We hope to improve our classification method in the future to allow for a fully automatic and robust eigenmode classification procedure.

ACKNOWLEDGEMENTS

Work supported by the Spanish MINECO (grant AYA2015-66899-C2-1-P), by the Generalitat Valenciana (PROMETEOII-2014-069) and by the European Gravitational Observatory (EGO-DIR-51-2017). P.C. acknowledges the support from the Ramon y Cajal program of the Spanish MINECO (RYC-2015-19074). A.P. acknowledges support from the European Union under the Marie Skłodowska Curie Actions Individual Fellowship, grant agreement no 656370. J.A.F. acknowledges support from the European Union's Horizon 2020 RISE programme H2020-MSCA-RISE-2017 Grant No. FunFiCO-777740.

REFERENCES

- Abbott B. P., et al., 2017a, *Nature*, 551, 85
 Abbott B. P., et al., 2017b, *ApJ*, 848, L12
 Abbott B. P., et al., 2017c, *Astrophys. J.*, 848, L13
 Abbott B. P., et al., 2017d, *Astrophys. J.*, 850, L39
 Abbott B. P., et al., 2018, preprint, ([arXiv:1805.11581](https://arxiv.org/abs/1805.11581))
 Aduara J. E., Cordero-Carrión I., Cerdá-Durán P., Aloy M. A., 2016, *Journal of Computational Physics*, 321, 369
 Andresen H., Müller B., Müller E., Janka H.-T., 2017, *MNRAS*, 468, 2032
 Annala E., Gorda T., Kurkela A., Vuorinen A., 2018, *Physical Review Letters*, 120, 172703
 Arfken G. B., Weber H. J., 1995, *Mathematical methods for physicists*; 4th ed.. Academic Press, San Diego, CA, <https://cds.cern.ch/record/379118>
 Banyuls F., Font J. A., Ibáñez J. M., Martí J. M., Miralles J. A., 1997, *ApJ*, 476, 221
 Blanchet L., Damour T., Schaefer G., 1990, *MNRAS*, 242, 289
 Blondin J. M., Mezzacappa A., DeMarino C., 2003, *ApJ*, 584, 971

Camelio G., Lovato A., Gualtieri L., Benhar O., Pons J. A., Ferrari V., 2017, preprint, ([arXiv:1704.01923](https://arxiv.org/abs/1704.01923))

Cerdá-Durán P., Faye G., Dimmelmeier H., Font J. A., Ibáñez J. M., Müller E., Schäfer G., 2005, *A&A*, **439**, 1033

Cerdá-Durán P., DeBrye N., Aloy M. A., Font J. A., Obergaulinger M., 2013, *ApJ*, **779**, L18

Chandrasekhar S., 1964, *ApJ*, **140**, 417

Cordero-Carrión I., Cerdá-Durán P., Dimmelmeier H., Jaramillo J. L., Novak J., Gourgoulhon E., 2009, *Phys. Rev. D*, **79**, 024017

Cowling T. G., 1941, *MNRAS*, **101**, 367

Cox J. P., 1980, Theory of stellar pulsation

De S., Finstad D., Lattimer J. M., Brown D. A., Berger E., Biwer C. M., 2018, preprint, ([arXiv:1804.08583](https://arxiv.org/abs/1804.08583))

Dimmelmeier H., Font J. A., Müller E., 2002, *A&A*, **388**, 917

Dimmelmeier H., Novak J., Font J. A., Ibáñez J. M., Müller E., 2005, *Phys. Rev. D*, **71**, 064023

Eckart C., 1960, Hydrodynamics of Oceans and Atmospheres

Fatoyev F. J., Piekarewicz J., Horowitz C. J., 2018, *Physical Review Letters*, **120**, 172702

Ferrari V., Miniutti G., Pons J. A., 2003, *MNRAS*, **342**, 629

Ferrari V., Gualtieri L., Pons J. A., Stavridis A., 2004, *Classical and Quantum Gravity*, **21**, S515

Foglizzo T., 2002, *A&A*, **392**, 353

Foglizzo T., Galletti P., Scheck L., Janka H.-T., 2007, *ApJ*, **654**, 1006

Friedman J. L., Stergioulas N., 2013, Rotating Relativistic Stars. Cambridge Monographs on Mathematical Physics, Cambridge University Press, doi:10.1017/CBO9780511977596

Fryer C. L., New K. C. B., 2011, *Living Reviews in Relativity*, **14**, 1

Gossan S. E., Sutton P., Stuver A., Zanolin M., Gill K., Ott C. D., 2016, *Phys. Rev. D*, **93**, 042002

Isenberg J. A., 2008, *International Journal of Modern Physics D*, **17**, 265

Just O., Obergaulinger M., Janka H.-T., 2015, *MNRAS*, **453**, 3386

Kley W., Schäfer G., 1999, *Phys. Rev. D*, **60**, 027501

Klimenko S., et al., 2016, *Phys. Rev. D*, **93**, 042004

Kokkotas K. D., Schmidt B. G., 1999, *Living Reviews in Relativity*, **2**, 2

Krüger C. J., Ho W. C. G., Andersson N., 2015, *Phys. Rev. D*, **92**, 063009

Kuroda T., Kotake K., Takiwaki T., 2016, *ApJ*, **829**, L14

Lattimer J. M., Swesty F. D., 1991, *Nuclear Physics A*, **535**, 331

Marek A., Dimmelmeier H., Janka H.-T., Müller E., Buras R., 2006, *A&A*, **445**, 273

Morozova V., Radice D., Burrows A., Vartanyan D., 2018, preprint, ([arXiv:1801.01914](https://arxiv.org/abs/1801.01914))

Müller B., Janka H.-T., Marek A., 2013, *ApJ*, **766**, 43

Murphy J. W., Ott C. D., Burrows A., 2009, *ApJ*, **707**, 1173

Obergaulinger M., Just O., Aloy M. Á., 2018, *J. Phys. G. in press*,

Osaki J., 1975, *PASJ*, **27**, 237

Ott C. D., Dimmelmeier H., Marek A., Janka H.-T., Zink B., Hawke I., Schnetter E., 2007a, *Classical and Quantum Gravity*, **24**, S139

Ott C. D., Dimmelmeier H., Marek A., Janka H.-T., Hawke I., Zink B., Schnetter E., 2007b, *Physical Review Letters*, **98**, 261101

Passamonti A., Bruni M., Gualtieri L., Sopuerta C. F., 2005, *Phys. Rev. D*, **71**, 024022

Reisenegger A., Goldreich P., 1992, *ApJ*, **395**, 240

Scuflaire R., 1974, *A&A*, **36**, 107

Shibata M., Sekiguchi Y.-I., 2004, *Phys. Rev. D*, **69**, 084024

Sotani H., Takiwaki T., 2016, *Phys. Rev. D*, **94**, 044043

Steiner A. W., Hempel M., Fischer T., 2013, *ApJ*, **774**, 17

Takata M., 2012, *PASJ*, **64**, 66

Thorne K. S., 1969, *ApJ*, **158**, 997

Thorne K. S., Campolattaro A., 1967, *ApJ*, **149**, 591

Thrane E., Coughlin M., 2015, *Physical Review Letters*, **115**, 181102

Torres-Forné A., Cerdá-Durán P., Passamonti A., Font J. A., 2018, *MNRAS*, **474**, 5272

Unno W., Osaki Y., Ando H., Shibahashi H., 1979, Nonradial oscillations of stars

Wilson J. R., Mathews G. J., Marronetti P., 1996, *Phys. Rev. D*, **54**, 1317

Woosley S. E., Bloom J. S., 2006, *ARA&A*, **44**, 507

Woosley S. E., Heger A., 2006, *ApJ*, **637**, 914

Woosley S. E., Heger A., 2007, *Phys. Rep.*, **442**, 269

Yakunin K. N., et al., 2015, *Phys. Rev. D*, **92**, 084040

APPENDIX A: COEFFICIENTS OF THE PERTURBATIVE EQUATIONS

The system of equations described in Sections 2.1 and 2.2 (for $l \neq 0$ and $l = 0$, respectively) can be cast in a matrix form as

$$\partial_r \mathbf{u} = \mathbf{A} \mathbf{u}. \quad (\text{A1})$$

For $l \neq 0$, $\mathbf{u} \equiv (\eta_r, \eta_\perp, K, \delta \hat{Q}, \Psi, \delta \hat{\psi})^T$ and the non-zero elements of \mathbf{A} are given by

$$A_{11} = -\frac{2}{r} - \frac{\mathcal{G}}{c_s^2} - 6 \frac{\partial_r \psi}{\psi},$$

$$A_{12} = \frac{\psi^4}{\alpha^2 c_s^2} (\mathcal{L}^2 - \sigma^2),$$

$$A_{14} = \frac{1}{c_s^2 Q},$$

$$A_{16} = -\left(6 + \frac{1}{c_s^2}\right) \frac{1}{\psi},$$

$$A_{21} = \left(1 - \frac{\mathcal{N}^2}{\sigma^2}\right),$$

$$A_{22} = -\partial_r \ln q + \mathcal{G} \left(1 + \frac{1}{c_s^2}\right),$$

$$A_{24} = \frac{\alpha}{\psi^5 \sigma^2} \left[\partial_r (\ln \rho h) - \left(1 + \frac{1}{c_s^2}\right) \mathcal{G} \right],$$

$$A_{26} = -\frac{\alpha^2}{\psi^5 \sigma^2} \left[-\partial_r (\ln \rho h) + \left(1 + \frac{1}{c_s^2}\right) \mathcal{G} \right] = -\alpha A_{24},$$

$$A_{31} = -2\pi \rho h \alpha \psi^5 \mathcal{B},$$

$$A_{32} = 2\pi \rho h \alpha \psi^5 \left(6 + \frac{1}{c_s^2}\right) \frac{\psi^4 \sigma^2}{\alpha^2},$$

$$A_{33} = -\frac{2}{r},$$

$$A_{34} = \frac{l(l+1)}{r^2} - 2\pi \psi^4 \left(5e + \frac{\rho h}{c_s^2}\right),$$

$$A_{36} = 2\pi \psi^4 \alpha \left[10e + 30P + \frac{\rho h}{c_s^2} \right],$$

$$A_{43} = 1,$$

$$A_{51} = 2\pi\rho h\psi^5\mathcal{B},$$

$$A_{52} = -2\pi\rho h\psi^5\frac{\psi^4\sigma^2}{\alpha^2c_s^2},$$

$$A_{54} = 2\pi\psi^4\frac{\rho h}{\alpha c_s^2},$$

$$A_{55} = -\frac{2}{r},$$

$$A_{56} = \frac{l(l+1)}{r^2} - 2\pi\psi^4\left(5e + \frac{\rho h}{c_s^2}\right),$$

$$A_{65} = 1.$$

For $l = 0$, $\mathbf{u} \equiv (\eta_r, \delta\hat{P}, K, \delta\hat{Q}, \Psi, \delta\hat{\psi})^T$ and the non-zero elements of \mathbf{A} are

$$A_{11} = -\frac{2}{r} - \frac{\mathcal{G}}{c_s^2} - 6\frac{\partial_r\psi}{\psi},$$

$$A_{12} = -\frac{1}{\rho h c_s^2},$$

$$A_{16} = -\frac{6}{\psi},$$

$$A_{21} = -q(\mathcal{N}^2 - \sigma^2),$$

$$A_{22} = \mathcal{G}\left(1 + \frac{1}{c_s^2}\right),$$

$$A_{23} = -\rho h\alpha^{-1}\psi^{-1},$$

$$A_{24} = \rho h\alpha^{-1}\psi^{-1}(\partial_r \ln \psi - \mathcal{G}),$$

$$A_{25} = \rho h\psi^{-1},$$

$$A_{26} = -\rho h\psi^{-1}(\partial_r \ln \psi),$$

$$A_{31} = -2\pi\rho h\alpha\psi^5\mathcal{B},$$

$$A_{32} = 2\pi\alpha\psi^5\left(6 + \frac{2}{c_s^2}\right),$$

$$A_{33} = -\frac{2}{r},$$

$$A_{34} = 2\pi\psi^4(\rho h + 5P),$$

$$A_{36} = 8\pi\alpha\psi^4(\rho h + 5P),$$

$$A_{43} = 1,$$

$$A_{51} = 2\pi\rho h\psi^5\mathcal{B},$$

$$A_{52} = -2\pi\psi^5\frac{1}{c_s^2},$$

$$A_{55} = -\frac{2}{r},$$

$$A_{56} = -10\pi\psi^4e,$$

$$A_{65} = 1.$$

APPENDIX B: ALTERNATIVE NUMERICAL METHOD

We have also computed the eigenmodes using an alternative numerical method. Instead of solving the system of 6 coupled ODEs, we solve a system of 2 ODEs for the fluid variables (η_r and η_\perp for the case $l \neq 0$, or η_r and $\delta\hat{P}$ for $l = 0$) coupled

with two elliptic equations for the metric perturbations $\delta\hat{\psi}$ and $\delta\hat{Q}$ (Eqs. (37) and (38) for $l \neq 0$ or Eqs. (47) and (48) for $l = 0$).

Each of the metric equations, as well as the corresponding boundary conditions given by Eqs. (54)-(55) are discretised to second order accuracy and written as two linear systems of equations that are solved using the LAPACK library³. Details on the implementation and tests of the elliptic solver can be found in [Adsuaru et al. \(2016\)](#). Since the metric equations and the fluid equations are coupled, we obtain the solution of the system of four equations (for each value of σ) in an iterative way. We first integrate the fluid variables considering $\delta\hat{Q} = \delta\hat{\psi} = 0$ (Cowling), then we use the values of their values to compute the metric perturbations, and continue with the iteration until the residual of all four quantities, computed as the L2 norm of the difference between two consecutive iterations is below 10^{-4} . For most of the values of σ , this procedure converges to a solution in less than ~ 10 iterations. Below a certain threshold in the value of σ , the iterative procedure becomes unstable and no convergence is achieved, even using a small relaxation factor in the iteration. The reason is that towards lower values of σ , there appear g-modes with increasing number of nodes. For sufficiently low values of σ , the g-modes have a number of nodes comparable to the number of grid points and this triggers point-to-point numerical noise, which spoils the solution. However, this is not a limitation of our method, because it only affects the calculation of very high-order g-modes (typically above order 10), which are not relevant to GW observations (see discussion in Section 5.3 in [Torres-Forné et al. 2018](#)) and are not well resolved in simulations, anyway.

We have compared the eigenmodes computed with this alternative method with the ones given in the main text. The discrepancy in the eigenfrequencies is in all cases below 0.1%. Given that the alternative method becomes numerically unstable in some cases and does not improve the solution, we only present results obtained with our main method in this work.

APPENDIX C: EIGENFUNCTION CLASSIFICATION PROCEDURE

We describe in this appendix the steps that we carry out to classify the eigenmodes of our linear analysis. This classification is based on the similarity with the modes from previous time steps.

(i) For each mode at each time, we interpolate linearly the values of η_r and η_\perp (and all necessary quantities) to an equally spaced grid of 300 points between the centre and the shock location. Instead of the radial coordinate we use a rescaled coordinate $x \in [0, 1]$, which maps the interval $r \in [0, r_{\text{core}}]$ to $x \in [0, 1/3]$, the interval $r \in [r_{\text{core}}, r_{\text{pns}}]$ to $x \in [1/3, 2/3]$ and the interval $r \in [r_{\text{pns}}, r_{\text{shock}}]$ to $x \in [2/3, 1]$, where r_{core} , r_{pns} and r_{shock} are the radial location of the core surface, the PNS surface and the shock.

³ Linear Algebra PACKage library, <http://www.netlib.org/lapack/>.

(ii) We normalise the eigenfunctions such that all have the same mean energy density, $E/V = 1$, where E is the energy of the mode, given by Eq. (58), and V is the volume of the region inside the shock. In this way, the eigenfunctions at different times are easier to compare with each other.

(iii) Next, we count the number of interior nodes (not counting the ones at the centre and at the shock) by searching for changes in the sign of η_r . This information can be used to classify the modes according to the Cowling or ESO classification schemes, and serves as a guide here.

(iv) We compute the energy density of each mode, $\mathcal{E}(x)$, using Eq. (59). Our matching algorithm is based on the similarity of this function at different times. This quantity has some advantages with respect to the eigenfunctions itself. Firstly, it is a combination of the radial and perpendicular parts, and secondly it is a positive function and does not suffer from the sign ambiguity that the eigenfunctions have.

(v) Our matching algorithm serves to identify a series of modes at different times as members of the same class. However, it does not give a name for the class. We use the ESO classification at the starting point of the algorithm to give a preliminary tag for the modes. In most of the cases we applied our matching procedure backward in time, using as starting point the last time output (the exception being the $l = 0$ modes). For each of the identified modes, ${}^l m_n$, with $m = \{f, p, g, h\}$ denoting the possible mode classes, we create a template $\mathcal{E}(r; {}^l m_l)$ as a basis for comparison.

(vi) We proceed to the next time output and we compare all the templates with the energy density of the new eigenmodes $\mathcal{E}(r; \sigma)$, where σ belongs to all possible eigenvalues of the new time output. For all possible values of σ and ${}^l m_n$ (for the same l) we compute the L2-norm of the difference

$$L2(\sigma | {}^l m_n) \equiv \sum_{i=1}^N \left(\mathcal{E}(x_i; {}^l m_n) - \mathcal{E}(x_i; \sigma) \right)^2. \quad (\text{C1})$$

Values of $L2(\sigma | {}^l m_n) \ll 1$, indicate a good matching between the eigenfunction corresponding to σ and the template for ${}^l m_n$.

(vii) We restrict our comparison to frequencies σ which are close to the sequence corresponding to the template ${}^l m_n$. To do this, we extrapolate the sequence of the modes already classified as ${}^l m_n$ to the new time and compare this value with σ . If the relative difference is larger than a certain threshold (10 – 20%) we reject this combination as possible. We use linear extrapolation in this procedure for the model 35OC and constant extrapolation for the s20. The extrapolation function is a least squares fit to the last 10–20 points already classified.

(viii) We order all possible matching combinations of modes in ascending order (better to worse matching) and assign sequentially to each unclassified mode a class given by the corresponding matching template. Modes already classified are removed from the sequence to avoid repetitions.

(ix) If there are unclassified modes, we use them to create new templates using the ESO criterium.

(x) We update the templates incorporating the information of the newly classified eigenfunction and repeat the process for the next time output. For p- and f-mode sequences, the template is a mean of the last 10 classified modes. This allows for smooth variations in the form of the eigenfunction over time, in particular the location of the nodes. For

g-modes, which evolve more slowly in time, we use all previously classified modes.

Once all modes have a preliminary classification, we perform some modifications to improve the matching:

(i) For f- and p-modes, we reorder the frequencies according to the number of radial nodes at each frequency, such that higher order modes have more nodes. This solves some misclassification issues of high order p-modes.

(ii) We retag manually some of the low order modes such that the time evolution of the profiles of \mathcal{E} is similar to the corresponding modes in the decoupled case (see Section 3.3.3), and that the p-modes are approximately integer multiples of the f-mode.

Note that the classification is not fully automatic as it requires the adjustment of a few parameters and thresholds and the manual retag at the end, for each of the models.

This paper has been typeset from a $\text{\TeX}/\text{\LaTeX}$ file prepared by the author.